The Astrophysical Journal, 885:28 (23pp), 2019 November 1 https://doi.org/10.3847/1538-4357/ab3eb6

Integrated Spectra of Milky Way Globular Clusters

T. C. Moura[1], M. Trevisan[2], B. Barbuy[1], and S. Rossi[1]
[1] Universidade de São Paulo, IAG, Rua do Matão 1226, Cidade Universitária, São Paulo 05508-900, Brazil
[2] Universidade Federal do Rio Grande do Sul, Departamento de Astronomia, CP 15051, Porto Alegre 91501-970, Brazil
Received 2019 July 16; revised 2019 August 20; accepted 2019 August 26; published 2019 October 25

Abstract

Integrated spectra of Milky Way globular clusters (GCs) are reproduced by computing synthetic spectra taking into account individual element abundances. Five clusters were selected from their location in the Galactic bulge, for which integrated spectra were available in the WiFeS Atlas of Galactic Globular Cluster Spectra project. Our aim is to further study the oldest GCs located in the Galactic bulge, with a metallicity in the range $-1.6 <$ [Fe/H] < -0.7. We also include the halo cluster NGC 6752 for comparison purposes. We reproduce the full spectra in the range 4500–9000 Å available in these observed spectra, as well as individual lines of Na, Mg, Al, Si, Ca, Ti, Ba, and Eu. We report a list of lines that are suitable for abundance derivation, and by adopting these abundances, we are able to fit the damping parameters that define the wings of strong lines of well-known triplets of Mg I and Ca II. Finally, the effect of multiple stellar populations through enhanced Na abundances is tested.

Unified Astronomy Thesaurus concepts: Galactic bulge (2041); Globular star clusters (656); Galaxy abundances (574); Stellar atmospheres (1584); Stellar populations (1622)

1. Introduction

Integrated spectra of Milky Way (MW) globular clusters (GCs) are becoming an increasingly important ingredient in the study of faint and compact GCs in our Galaxy and in other galaxies, as well as the integrated spectra of galaxies.

The integrated spectra of MW GCs observed by Bica & Alloin (1986), Schiavon et al. (2005), and Usher et al. (2017) offer an important basis for the validation of codes that try to reproduce integrated spectra of star clusters and old galaxies.

At the same time, given the degeneracy between metallicity and age, in order to reproduce the integrated spectra, it is best to have input data on ages and chemical abundances, which is possible for MW and Magellanic Cloud GCs. Compilations of such data for the MW were presented by Pritzl et al. (2005) and Harris (1996, 2010 edition).[3] In a series of papers, Saviane et al. (2012), Dias et al. (2015, 2016), and Vásquez et al. (2018) derived abundances and alpha-to-iron ratios from FORS2@VLT spectra for individual stars in 61 GCs, targeting less well-studied ones, and compared them with the literature.

Work on derivation of abundances from integrated spectra is becoming available for the old GCs in the Galaxy, where ages from the literature are adopted. Roediger et al. (2014) derived abundances from the integrated spectra of 41 GCs for which Schiavon et al. (2005) had obtained the integrated spectra. Sakari et al. (2013) and Colucci et al. (2017, and references therein) were able to measure equivalent widths (EWs) and derive abundances. Larsen et al. (2017, and references therein) and Conroy et al. (2018, and references therein) were able to derive metallicities and abundances from full spectrum fitting of the integrated spectra of GCs.

A recent review on the building of integrated spectra for single stellar populations (SSPs) is presented by Martins et al. (2019). They investigate the methods and ingredients used, including differences between evolutionary tracks or use of observed color–magnitude diagrams (CMDs), initial mass functions (IMFs), and spectral libraries available in the literature.

In the present work, we use spectra from the WiFeS Atlas of Galactic Globular Cluster Spectra (WAGGS) project by Usher et al. (2017), that made available integrated spectra of a series of GCs. We have selected for our analysis, six GCs from Usher et al. (2017) that have good signal-to-noise ratios (S/Ns), where five of them are contained in the list of 43 bulge GCs as selected by Bica et al. (2016), and additionally, the halo cluster NGC 6752, for comparisons with the literature. We also limited the metallicity to be within $-1.6 <$ [Fe/H] < -0.7, in order to concentrate efforts on the oldest GCs of the Galactic bulge.

For the building of the integrated spectra, we here describe in detail the code SynSSP. In this code we adopt the Dartmouth (Dotter et al. 2008) isochrones, and compute the spectra of a series of stars along the main-sequence (MS), subgiant, and red giant phases, for a given age, metallicity, [α/Fe], and element abundances. The synthetic spectra are computed in each run. A previous version of this procedure was already described in La Barbera et al. (2013). The code is now much improved, mainly due to the update of the code PFANT for spectrum synthesis, as described in Barbuy et al. (2018b). The code was entirely upgraded with homogeneization of language to Fortran 2003, optimization for speed, and improved error reporting in case of problems with the input data files. Line lists were also revised.

The ages are adopted from the recent age derivations by Kerber et al. (2018), R. A. P. Oliveira et al. (2019, in preparation), and VandenBerg et al. (2013), from isochrone fitting to CMDs. Our main interest is to reproduce the integrated spectra by computing stellar spectra taking into account their elemental abundances, reported in high-resolution spectroscopic studies, and by further deriving element abundances from the integrated spectra.

We also investigate the multiple stellar populations, in proportions derived by Milone et al. (2017) and R. A. P. Oliveira et al. (2019, in preparation), by analyzing the effect of a combined spectrum of first and second generations, with different Na abundances. The use of Na and TiO line intensities to deduce a bottom-heavy stellar IMF is also discussed.

[3] www.physics.mcmaster.ca/~harris/mwgc.dat

Table 1
Galactic Coordinates, Distances to the Sun and to the Galactic Center, Absolute Visual Magnitude from Harris (1996), Fraction of First Generation Stars from Milone et al. (2017), Ages from R. A. P. Oliveira et al. (2019, in preparation) for NGC 6624, NGC 6637, and NGC 6723, Ages from Kerber et al. (2018) for NGC 6522, and Ages from VandenBerg et al. (2013) for NGC 6171 and NGC 6752

Cluster	l (°)	b (°)	$d_{\odot}$ (kpc)	d_{GC} (kpc)	M_V	N_1/N_{TOT}	Age (Gyr)	$\delta Y_{1G,2G}$
NGC 6171	3.37	23.01	6.4	3.3	−7.12	0.397	12.0	0.019
NGC 6522	1.02	−3.93	7.7	0.6	−7.95	0.160	13.0	⋯
NGC 6624	2.79	−7.91	7.9	1.2	−7.49	0.279	12.5	0.010
NGC 6637	1.72	−10.27	8.8	1.7	−7.64	0.425	12.4	0.004
NGC 6723	0.07	−17.30	8.7	2.6	−7.83	0.363	12.5	0.005
NGC 6752	336.49	−25.63	4.0	5.2	−7.73	0.294	12.5	0.010, 0.032

Note. Y are helium enhancements in second generation stars (third for the case of NGC 6752) from Milone et al. (2018, 2019).

Table 2
Literature Metallicities and Abundances for the Sample Clusters

Cluster	[Fe/H]	[O/Fe]	[Na/Fe]	[Al/Fe]	[Mg/Fe]	[Si/Fe]	[Ca/Fe]	[Ti/Fe]	[Ba/Fe]	[Eu/Fe]	Method	References
NGC 6171	−1.02	+0.17	+0.37	⋯	+0.51	+0.54	+0.06	+0.40	⋯	⋯	comp.	Roediger et al. (2014)
	−1.02	⋯	⋯	⋯	+0.41	+0.25	+0.32	+0.42	⋯	⋯	ISFF	Conroy et al. (2018)
	−1.58	⋯	⋯	⋯	⋯	⋯	+0.24	⋯	⋯	⋯	ISEW	Usher et al. (2019)
NGC 6522	−0.95	+0.36	+0.05	+0.20	+0.23	+0.13	+0.13	+0.04	+0.32	+0.30	HRS	Barbuy et al. (2014)
	−1.12	⋯	+0.24	+0.62	+0.42	+0.28	+0.35	+0.38	+0.37	+0.43	HRS	Ness et al. (2014)
(2G)	−1.04	+0.33	⋯	+0.57	+0.13	+0.30	⋯	⋯	⋯	⋯	HRS	Fernández-Trincado et al. (2019)
	−1.21	⋯	⋯	⋯	+0.47	+0.30	+0.35	+0.40	⋯	⋯	ISFF	Conroy et al. (2018)
	−1.58	⋯	⋯	⋯	⋯	⋯	+0.13	⋯	⋯	⋯	ISEW	Usher et al. (2019)
	−1.34	+0.49	+0.04	⋯	+0.27	+0.25	+0.17	+0.16	⋯	⋯	comp.	Roediger et al. (2014)
NGC 6624	−0.69	+0.41	⋯	+0.39	+0.42	+0.38	+0.40	+0.37	⋯	⋯	HRS	Valenti et al. (2011)
	−0.77	⋯	⋯	⋯	+0.36	+0.25	+0.23	+0.41	⋯	⋯	ISFF	Conroy et al. (2018)
	−1.58	⋯	⋯	⋯	⋯	⋯	+0.18	⋯	⋯	⋯	ISEW	Usher et al. (2019)
	−0.44	+0.41	⋯	⋯	+0.42	+0.38	+0.40	+0.37	⋯	⋯	comp.	Roediger et al. (2014)
NGC 6637	−0.77	+0.20	+0.35	+0.49	+0.28	+0.45	+0.20	+0.24	+0.22	+0.45	HRS	Lee (2007)
	−0.90	⋯	⋯	⋯	+0.43	+0.20	+0.30	+0.54	⋯	⋯	ISFF	Conroy et al. (2018)
	−1.58	⋯	⋯	⋯	⋯	⋯	+0.20	⋯	⋯	⋯	ISEW	Usher et al. (2019)
	−0.64	+0.20	+0.35	⋯	+0.28	+0.45	+0.20	⋯	⋯	⋯	comp.	Roediger et al. (2014)
NGC 6723	−0.98	+0.29	+0.00	0.31	+0.23	+0.36	+0.30	+0.24	+0.22	−	HRS	Rojas-Arriagada et al. (2016)
	−1.22	+0.39	+0.05	⋯	+0.58	⋯	⋯	⋯	⋯	⋯	HRS	Gratton et al. (2015) (BHB)
	−1.22	+0.55	+0.11	⋯	+0.50	+0.59	+0.81	⋯	+0.75	⋯	HRS	Gratton et al. (2015) (RHB)
(1G)	−0.91	+0.39	+0.14	+0.32	+0.47	+0.52	+0.37	+0.34	+0.36	+0.38	HRS	Crestani et al. (2019)
	−1.32	⋯	⋯	⋯	+0.53	+0.20	+0.33	+0.29	⋯	⋯	ISFF	Conroy et al. (2018)
	−1.58	⋯	⋯	⋯	⋯	⋯	+0.49	⋯	⋯	⋯	ISEW	Usher et al. (2019)
	−1.10	⋯	⋯	⋯	+0.44	+0.68	+0.33	+0.24	⋯	⋯	comp.	Roediger et al. (2014)
NGC 6752	−1.56	+0.16	+0.33	+0.41	+0.50	+0.38	⋯	⋯	⋯	⋯	HRS	Carretta et al. (2009)
(1G)	−1.56	+0.54	+0.01	+0.11	+0.45	+0.51	⋯	⋯	⋯	⋯	HRS	Carretta et al. (2012)
(2G)	−1.56	+0.25	+0.36	+0.74	+0.42	+0.48	⋯	⋯	⋯	⋯	HRS	Carretta et al. (2012)
(3G)	−1.56	+0.06	+0.62	+1.21	+0.31	+0.43	⋯	⋯	⋯	⋯	HRS	Carretta et al. (2012)
	−1.58	⋯	+0.09	⋯	⋯	⋯	+0.46	+0.36	+0.10	⋯	ISEW	Colucci et al. (2017)
	−1.58	⋯	⋯	⋯	⋯	⋯	+0.26	⋯	⋯	⋯	ISEW	Usher et al. (2019)
	−1.883	⋯	+0.302	⋯	+0.391	⋯	+0.355	+0.342	+0.182	⋯	ISFF	Larsen et al. (2017)
	−1.64	⋯	⋯	⋯	+0.54	+0.42	+0.33	+0.29	⋯	⋯	ISFF	Conroy et al. (2018)

In Section 2, the available literature on the sample clusters is reported. In Section 3, we describe the calculations of integrated spectra of simple stellar populations employed in this work. In Section 4. we examine individual abundances that can be derived from the integrated spectra. In Section 5, the effect of multiple stellar populations on Na lines is investigated. In Section 6, conclusions are drawn.

2. Sample GCs

Our sample is composed of five GCs in the Galactic bulge and one halo cluster in the metallicity range $-1.6 \lesssim$ [Fe/H] $\lesssim -0.7$, with ages older than 11 Gyr, and for which there are available integrated spectra in the WiFeS Atlas of Galactic Globular Cluster Spectra—WAGGS project from Usher et al. (2017). The integrated spectra from the WAGGS library were

Table 3
List of Lines Inspected in the Integrated Spectra, and Resulting Abundances

Species	λ (Å)	χ_{ex} (eV)	log gf	NGC 6171	NGC 6522	NGC 6624	NGC 6637	NGC 6723	NGC 6752
Na I	5682.633	2.10	−0.71	0.00 ± 0.15	0.00	0.20	0.00	⋯	0.00
Na I	5688.194	2.11	−1.40	0.35 ± 0.15	0.35	0.35	0.35	0.35	0.35
Na I	5688.205	2.11	−0.45	0.35 ± 0.15	0.35	0.35	0.35	0.35	0.35
Na I	6154.230	2.10	−1.56	0.35 ± 0.15	0.20	0.35	0.35	0.35	⋯
Na I	6160.753	2.10	−1.26	0.00 ± 0.15	0.00	0.35	0.00	0.35	0.35
Na I	8183.256	2.10	−0.47	0.35 ± 0.15	0.20	0.00	0.00	0.20	0.20
Na I	8194.790	2.10	+0.24	0.20 ± 0.15	0.20	0.20	0.00	0.00	0.35
Mg I	5528.405	4.34	−0.547	0.51 ± 0.15	0.23	0.42	0.28	0.23	0.38
Mg I	5711.088	4.34	−1.842	0.51 ± 0.10	0.23	0.42	0.28	0.45	0.25
Al I	6696.185	4.02	−1.58	0.25 ± 0.20	0.20	0.30	0.20	0.31	0.10
Al I	6696.204	4.02	−1.58	0.25 ± 0.20	0.20	0.30	0.20	0.31	0.10
Al I	6696.788	4.02	−1.42	0.25 ± 0.20	0.20	0.30	0.20	0.31	0.10
Al I	6698.673	3.14	−1.65	0.25 ± 0.20	0.20	0.30	0.20	0.31	0.10
Si I	6414.99	5.87	−1.13	0.47 ± 0.20	−0.05	0.15	0.45	−0.18	0.30
Si I	7405.79	5.61	−0.66	0.05 ± 0.20	−0.50	0.08	0.05	0.20	0.47
Si I	7415.96	5.61	−0.73	0.15 ± 0.20	0.20	0.38	0.25	0.20	0.47
Si I	7423.51	5.62	−0.58	0.05 ± 0.20	−0.18	0.08	0.05	−0.05	0.0
Ca I	6161.295	2.51	−1.02	0.21 ± 0.15	0.13	0.45	0.40	0.53	0.20
Ca I	6162.167	1.89	−0.09	0.21 ± 0.15	0.13	0.45	0.40	0.53	0.20
Ca I	6439.080	2.52	+0.3	0.21 ± 0.15	0.13	0.45	0.40	0.53	0.20
Ti I	5965.825	1.88	−0.42	−0.04 ± 0.10	0.04	0.37	0.24	0.24	0.20
Ti I	6261.106	1.43	−0.48	−0.04 ± 0.10	0.10	0.37	0.24	0.50	0.20
Ti I	6336.113	1.44	−1.74	−0.04 ± 0.10	0.04	0.37	0.24	0.24	0.20
Ba II	6496.90	0.604	−0.32	0.00 ± 0.15	0.02	0.10	0.22	0.22	0.00
Eu II	6645.064	1.38	+0.12	0.50 ± 0.15	0.55	0.00	0.45	0.00	0.50

Note. Uncertainties given for NGC 6171 are the same for all clusters for each respective line.

Table 4
Atomic Constants Adopted for the Mg I and Ca II Triplet Lines

Species	λ (Å)	χ_{ex} (eV)	log gf	C_6	γ_R/NH	γ_e/NH
Mg I	5167.3216	2.7091	−0.854 (1)	0.3E−29	1.0E+08	2.0E−07
Mg I	5172.684	2.7116	−0.363 (1)	idem	idem	idem
Mg I	5183.604	2.7166	−0.168 (1)	idem	idem	idem
Ca II	8498.023	1.6924	−1.312 (2)	0.9E−32	3.6E+08	2.6E−07
Ca II	8542.091	1.6999	−0.362 (2)	0.8E−32	3.0E+08	idem
Ca II	8662.141	1.6924	−0.623 (2)	0.8E−32	2.95E+08	idem

References. (1) Pehlivan Rhodin et al. (2017), (2) Kurúcz (2005).

observed with the WiFeS integral field spectrograph installed in the Australian National University 2.3 m telescope and cover a wide wavelength range from 3300–9050 Å at a spectral resolution of $R \sim 6800$.

Basic information on the selected GCs, including the galactic coordinates, distances to the Sun and to the Galactic center, and absolute magnitudes M_V from Harris (1996) are given in Table 1. In this table, the fractions of first generation (1G) stellar populations relative to the total, as estimated by Milone et al. (2017) from the *Hubble Space Telescope* ultraviolet filters, and ages deduced from Kerber et al. (2018), R. A. P. Oliveira et al. (2019, in preparation), and VandenBerg et al. (2013) are also given. Finally, He enhancements from a second generation (2G) relative to 1G from Milone et al. (2019) are listed. Literature chemical abundances derived with different methods are reported in Table 2.

3. Integrated Spectrum Model

In order to reproduce the integrated spectrum of a stellar population, the following ingredients are required: stellar evolutionary tracks and a library of stellar spectra. The isochrones determine the mass and the atmospheric parameters (surface gravity, log g, and effective temperatures, $T_{\rm eff}$) of stars belonging to an SSP with a given age, metallicity, and [α/Fe] enhancement. A number of stellar evolutionary stages are defined to be included in the synthesis, such that the integrated light spectrum of the SSP can be generated by combining the spectra of individual stars, according to a given IMF. In the present work, we assume a Salpeter IMF (Salpeter 1955), which is very similar with to Kroupa (2001) in the mass range of old stars.

Spectra of individual stars from empirical or synthetic libraries can be used. Given our aim of fitting particular lines by varying their abundances, empirical stellar libraries are not well suited for investigating how changes in the abundances of individual elements affect the spectral indices, since they are restricted to the abundance patterns of stars in the solar neighborhood.

For this reason, we developed the SynSSP package, which computes the spectra of SSPs with variable abundance ratios. The user can compute a synthetic SSP spectrum by providing some key parameters, as follows:

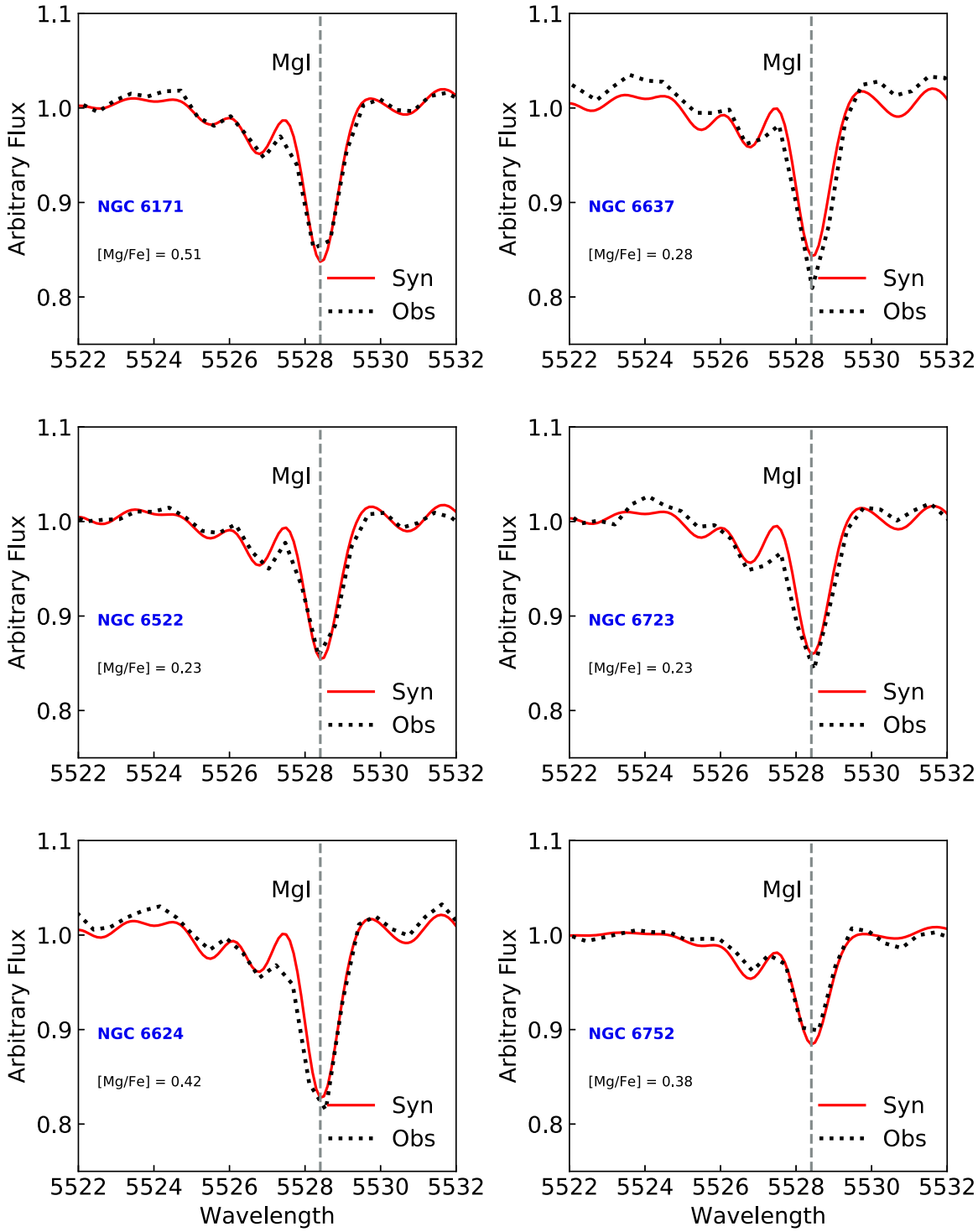

Figure 1. The observed and synthetic spectra for the Mg I line in 5528.405 Å line.

A. Stellar evolutionary ingredients:

1. Age, metallicity, and [α/Fe] of the SSP. We adopt the Dartmouth[4] stellar evolutionary tracks (Dotter et al. 2008). Primordial helium abundances are assumed.
2. Number of stars, characterized by their effective temperatures $T_{\rm eff}$, and surface gravity $\log g$, that should be selected along the isochrone. A standard procedure considers 12 stars in the main sequence (MS) and subgiant branch, and 9 stars in the red giant branch (RGB).

B. Synthetic stellar spectra:

1. A stellar synthetic spectrum is computed for each of the $T_{\rm eff}$ and $\log g$ pairs.
2. The values of [C, N, O, Na, Mg, Al, Si, Ca, Ti, Ba, and Eu/Fe] abundance ratios. Some default values are [C/Fe] $= -0.2$, [N/Fe] $= +1.0$, and [O, Mg, Si, Ca, Ti, Eu/Fe] $=$ [α/Fe]. For the other elements, literature or fitted

[4] http://stellar.dartmouth.edu/models/index.html

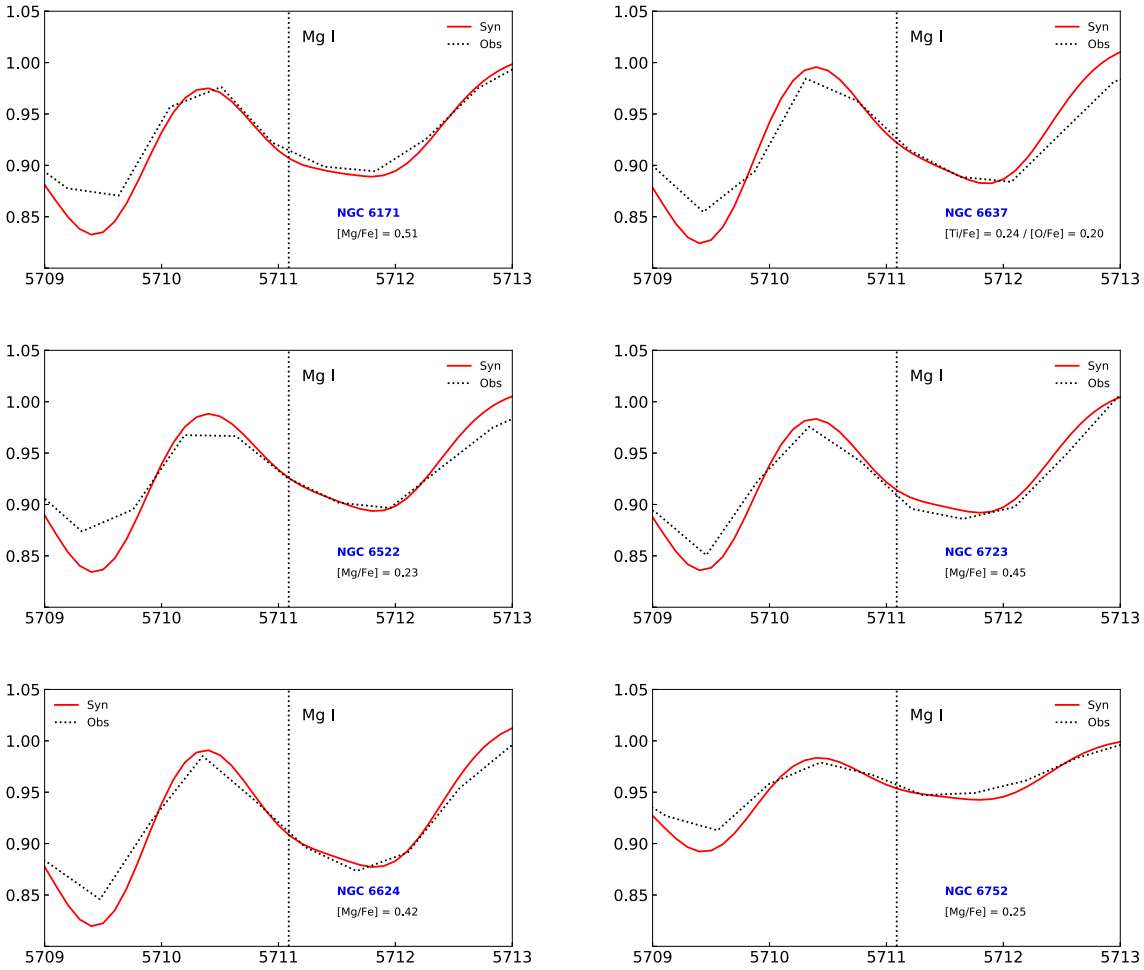

Figure 2. The Mg 5711.088 Å line for the sample clusters.

abundances are included, otherwise a solar abundance ratio is assumed.

3. The wavelength range being sampled, the spectral resolution of the computed spectra $\delta\lambda$, and the FWHM for convolution of the synthetic spectra. The default values are FWHM $= 0.2$ Å and $\delta\lambda = 0.1$ Å. In order to compare to the sample observed spectra, we used FWHM $= 1.0$ Å and $\delta\lambda = 0.5$ Å.

The synthetic stellar spectra are generated using the PFANT code described in Barbuy (1982), Cayrel et al. (1991), Barbuy et al. (2003), and Coelho et al. (2005), and are updated in Barbuy et al. (2018b). Given a stellar model atmosphere and lists of atomic and molecular lines, the code computes a synthetic spectrum assuming local thermodynamic equilibrium (LTE). The atomic line list is that of VALD3 (Ryabchikova et al. 2015). For some specific lines we used updated oscillator strengths, in particular for the Mg I triplet at 5167–5183 Å (Pehlivan Rhodin et al. 2017). The molecular line list calibrated through several stellar spectroscopic studies is described in Barbuy et al. (2018b). The MARCS LTE atmospheric models by Gustafsson et al. (2008) are employed.

For each star along the isochrone we compute the synthetic spectrum, taking into account the abundances derived from high-resolution spectroscopy initially, and, if needed, further fitting abundances for the line list given in Table 3.

C. Computation of the integrated spectra:

The spectra of the SSP are created using the following integral

$$f(\lambda) = \int_{m_1}^{m_2} s(\lambda, m)\phi(m)dm,$$

where $s(\lambda, m)$ is the spectrum of an individual star with mass m as a function of wavelength λ and $\phi(m)$ is the IMF.

The code reads a list of the stellar parameters $T_{\rm eff}$, log g, mass, and luminosity log $(L/L_{\odot})$, and the corresponding synthetic stellar spectra $S(\lambda, \text{mass})$, computed for each pair of $T_{\rm eff}$, log g. The stellar population is then divided into N mass bins, with a lower mass $m_1 = 0.08\ M_{\odot}$, and m_2 is the highest mass found in the isochrones being fitted.

The package that computes SSP spectra with variable chemical abundances is available under request.

The abundances are varied all together, which is important, due in particular to effects of some of them as electron donors. Fe, Al, and α-elements such as Ca, are electron donors, and if enhanced, they contribute to the increase of the continuum by H-. For this reason, it is important to enhance them at the same time. Therefore, our method is different from those by Conroy et al. (2018) or Trager et al. (1998), where each element is

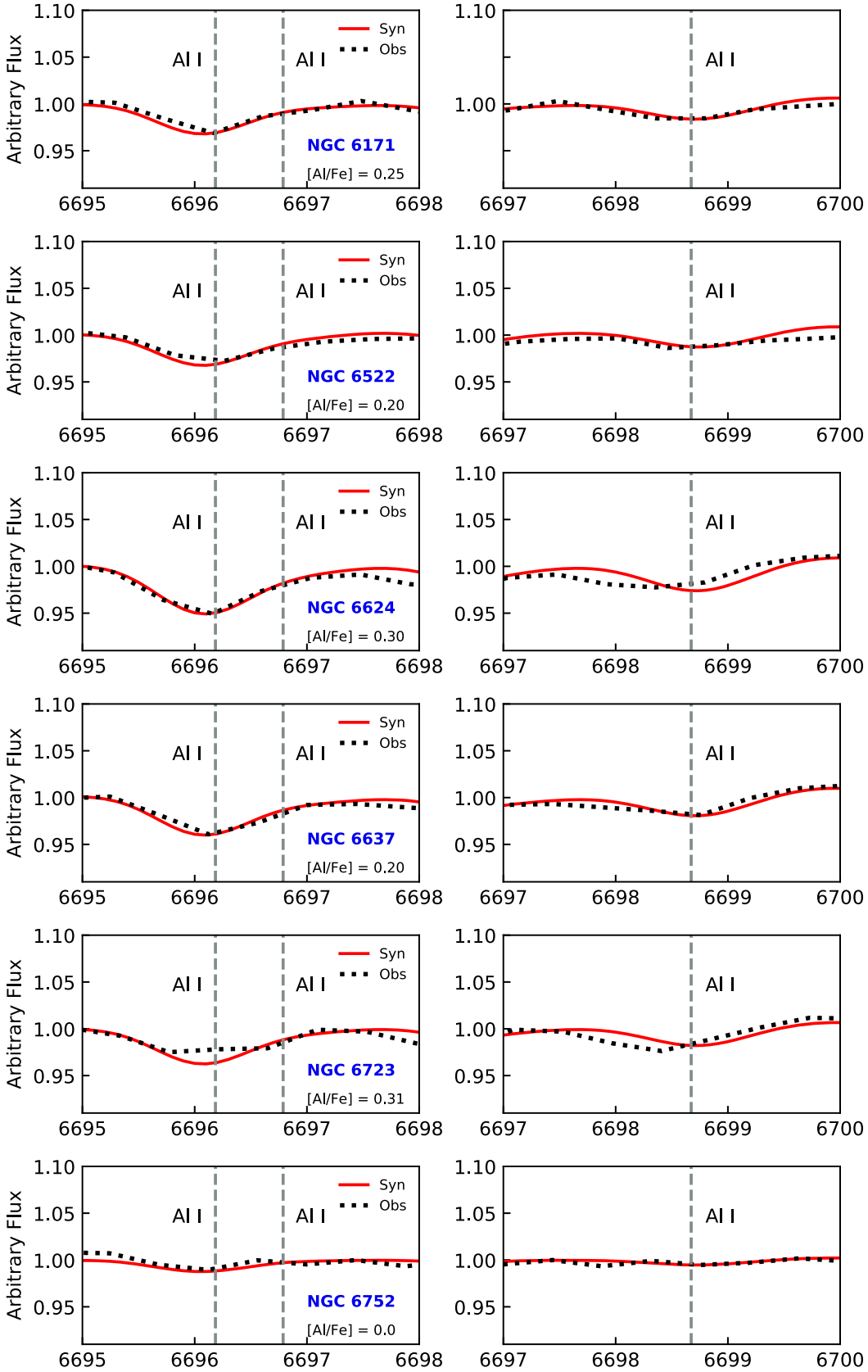

Figure 3. Observed and synthetic spectra in region of the Al I lines.

enhanced separately; it is also different from the method by Colucci et al. (2017) where the integrated spectra are analyzed by measuring EWs of lines.

Our method is more similar to that by Sakari et al. (2013) and Larsen et al. (2017, and references therein), consisting of full spectrum fitting, with the difference of us

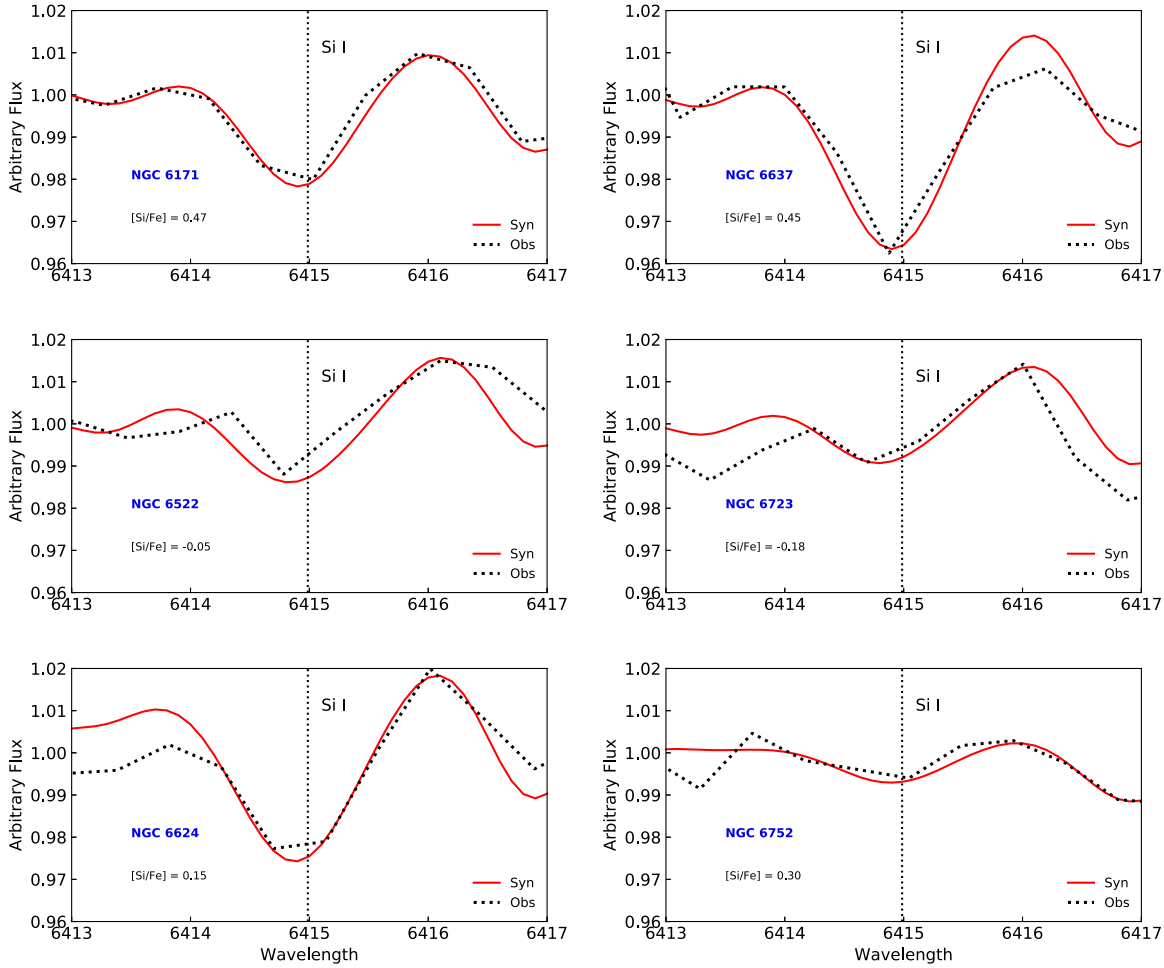

Figure 4. The synthetic and observed spectra for the six clusters of our sample in the region of the 6414.987 Å Si line.

fitting individual selected lines for element abundance derivation.

4. Reproduction of Integrated Spectra of Sample Clusters

We have computed integrated spectra for the six sample GCs, using the prescriptions described in the previous section. The overall fit in the wavelength range 4500–9000 Å is very satisfactory, as can be seen in Figures 15–19 in the Appendix, where where the full spectrum of NGC 6522 is fit. Residuals for regions of 100 Å were measured, and the resulting ratios between the synthetic and observed spectra are below 2%.

We further inspected suitable lines of interesting elements, for which we are able to fit element abundances. The fits to the selected lines, reported in Table 3, proceeded as in high-resolution spectroscopy, i.e., by fitting the local continuum, and finding the best abundance. For the strong lines (Table 4), the abundance is unchanged, because the bottom of these lines cannot be fitted in LTE, as discussed in Section 4.2.

4.1. Lines of Mg I, Na I, Al I, Si I, Ca I, Ti I, Ba II, and Eu II

In this subsection we present the resulting abundances from spectrum fitting for best lines for the elements Mg I, Na I, Al I, Si I, Ca I, Ti I, Ba II, and Eu II. The results are adopted as the element abundance in the sample clusters. The reason we prefer weaker lines rather than stronger lines to derive abundances is the simple fact that in that case the abundance increases linearly with EW (Gray 2005).

The fits to lines for all six clusters, for chosen lines of Na, Mg, Al, Si, Ca, Ti, Ba, and Eu, are described below. The element abundances obtained or adopted are given in the panels and gathered in Table 3. The Na lines and abundances are treated separately as reported in Section 5.

The uncertainties in the abundances derived in Table 3 are related to the strength of the line, and whether surrounding blends allow a good continuum fit. The uncertainties given in the table for NGC 6171 are adopted for all clusters for the same respective lines.

Mg I Lines—Figures 1 and 2 show the Mg I 5528.405 and 5711.08 Å lines that are well-fitted for the six clusters.

Al Lines—The Al I 6696.185, 6696.788, 6698.673 Å lines are shown in Figure 3. The calculations are in a good agreement with the integrated spectra, where for the clusters NGC 6723, NGC 6752, and NGC 6522, solar ratios are adopted. For NGC 6171, there are no Al abundances available in the literature. NGC 6171, NGC 6624, and NGC 6637 show Al enhancements that are also found in bulge field stars, where it behaves as an α-element (see McWilliam 2016; Barbuy et al. 2018a). Note that Al enhancements can also be an indicator of a second generation of stellar populations in GCs (Renzini et al. 2015; Bastian & Lardo 2018).

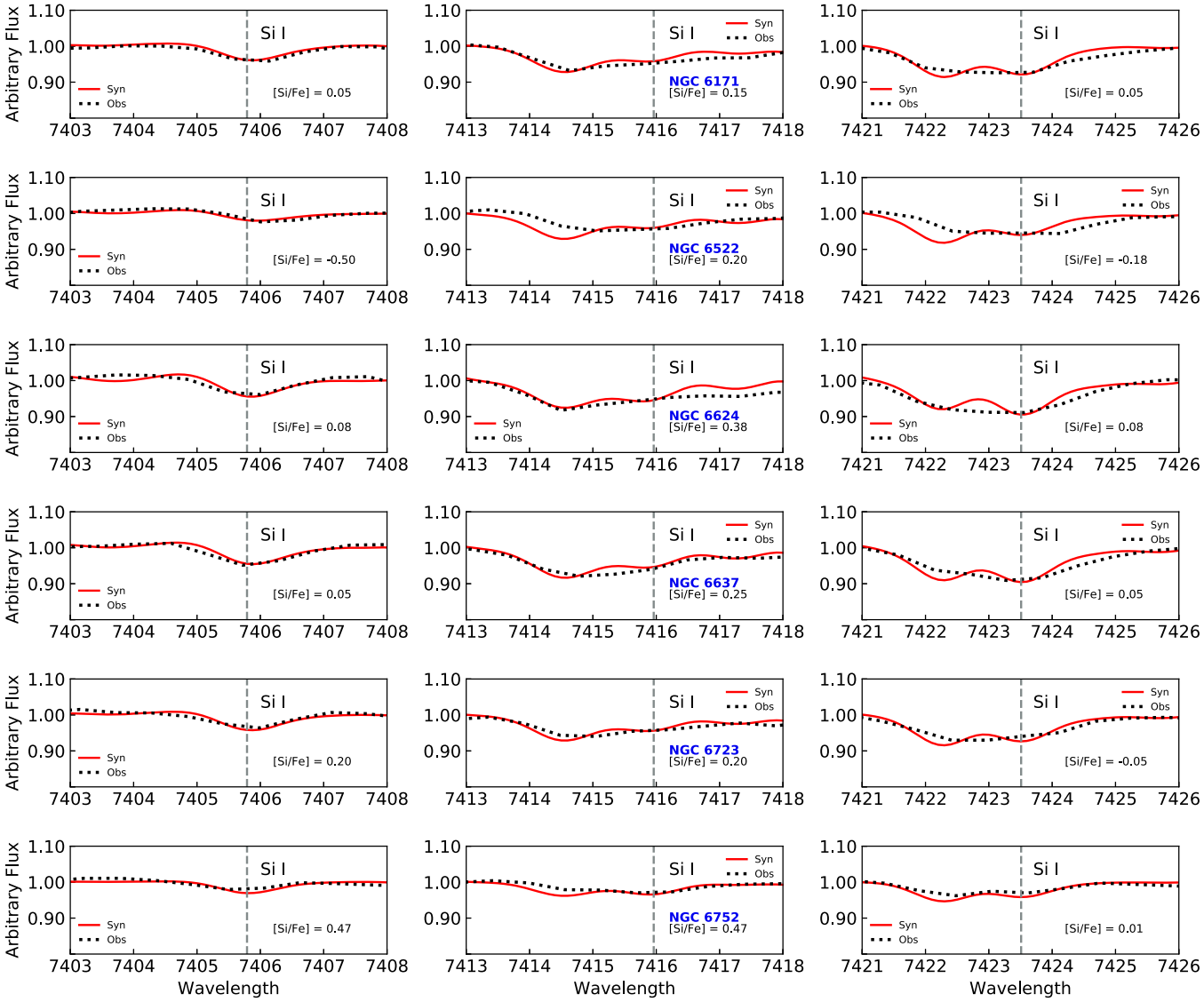

Figure 5. The 7405.79, 7415.9, and 7423.51 Å Si lines in the synthetic and observed spectra for our sample.

Si Lines—Figures 4 and 5 show the fits to the Si I 6414.99 and 7405.79 Å lines.

Ca Lines—Figure 6 shows the fits to the Ca I 6162.167 Å, as well as to the nearby Na I 6160.753 Å line, with the adopted abundances indicated in the figure and in Table 3. Usher et al. (2019) derived the Ca abundances for their full sample clusters, based on measurements of EWs with well-defined continua and the wavelength range of Ca II triplet lines (CaT). The values from Usher et al. (2019) and the present results are compatible (see Section 4.3). It is important to note that in this subsection we derived the Ca abundance from weak to medium lines, which are more suitable for abundance derivation, therefore a method different from Usher et al. (2019), even if using the same spectra. It is reassuring to conclude that the Ca abundances from the CaT strong lines measured as indices, and the fit to normally weak to medium lines in the integrated spectra, give very close results.

Ti Lines—Ti I 5965.825, 6261.106, and 6336.113 Å are used to derive Ti abundances, with the first two lines shown in Figure 7.

Ba lines—Figure 8 shows the fits to the Ba II 6496.897 Å line, with abundances indicated in the panels and in Table 3. Hyperfine structure (HFS) is taken into account following Barbuy et al. (2014).

Eu Line—Figure 9 gives the Eu II 6645.064 Å line well-fitted with literature abundances when available (NGC 6522 and NGC 6637), and for the others the line was fitted, with the resulting Eu abundance indicated in the figures, and in Table 3. HFS is taken into account.

4.2. Strong Mg I and Ca II Triplet Lines

For the strong lines of the Mg I triplet at 5167–5183 Å, and the Ca II triplet at 8498–8662 Å, we have adopted oscillator strengths from the recent literature, and derived astrophysical values for the damping constants to reproduce their wings, applied to the Sun and Arcturus. The abundances are adopted from the lines reported in Table 3.

The main mechanism of collisional broadening for metallic lines in stars of spectral types F and M is due to collisions with neutral hydrogen atoms. The damping constant γ for each

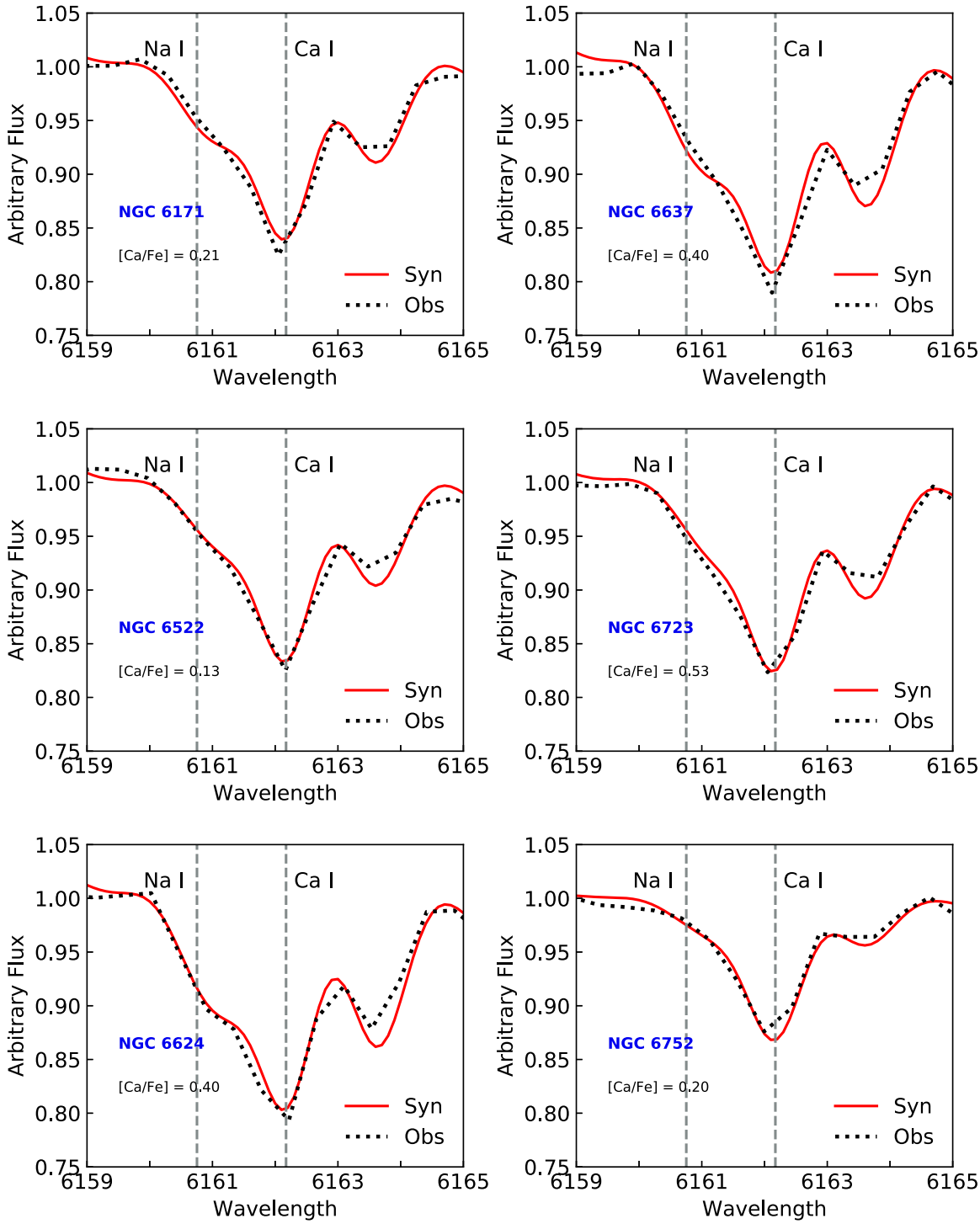

Figure 6. Observed and synthetic spectra in the region of the Ca I 6162.7 Å line.

atmospheric layer relates to the interaction constant C_6 as follows (Gray 2005):

$$\gamma_6/N_{\rm H} = 17 v^{3/5} C_6^{2/5}$$

where v is the relative velocity between the colliding particles and $N_{\rm H}$ is the density of hydrogen atoms.

The radiative broadening (taken as standard for most lines with $\gamma_{\rm R} = 2.21E15/\lambda^2$), as well as electron broadening are also taken into account, to form the final Voigt profile (Gray 2005). The values of $\gamma_{\rm R}$ and $\gamma_{\rm e}$ are adopted from the VALD3 (Ryabchikova et al. 2015) and Kurúcz webpage,[5] and these are further described in Smith & Drake (1988) and Chmielewski (2000).

The adopted values of the interaction constant, C_6, were obtained by adopting the recent literature oscillator strengths, and fitting of the wings. This is done by using the MARCS

[5] http://www.cfa.harvard.edu/amp/ampdata/kurucz23/sekur.html

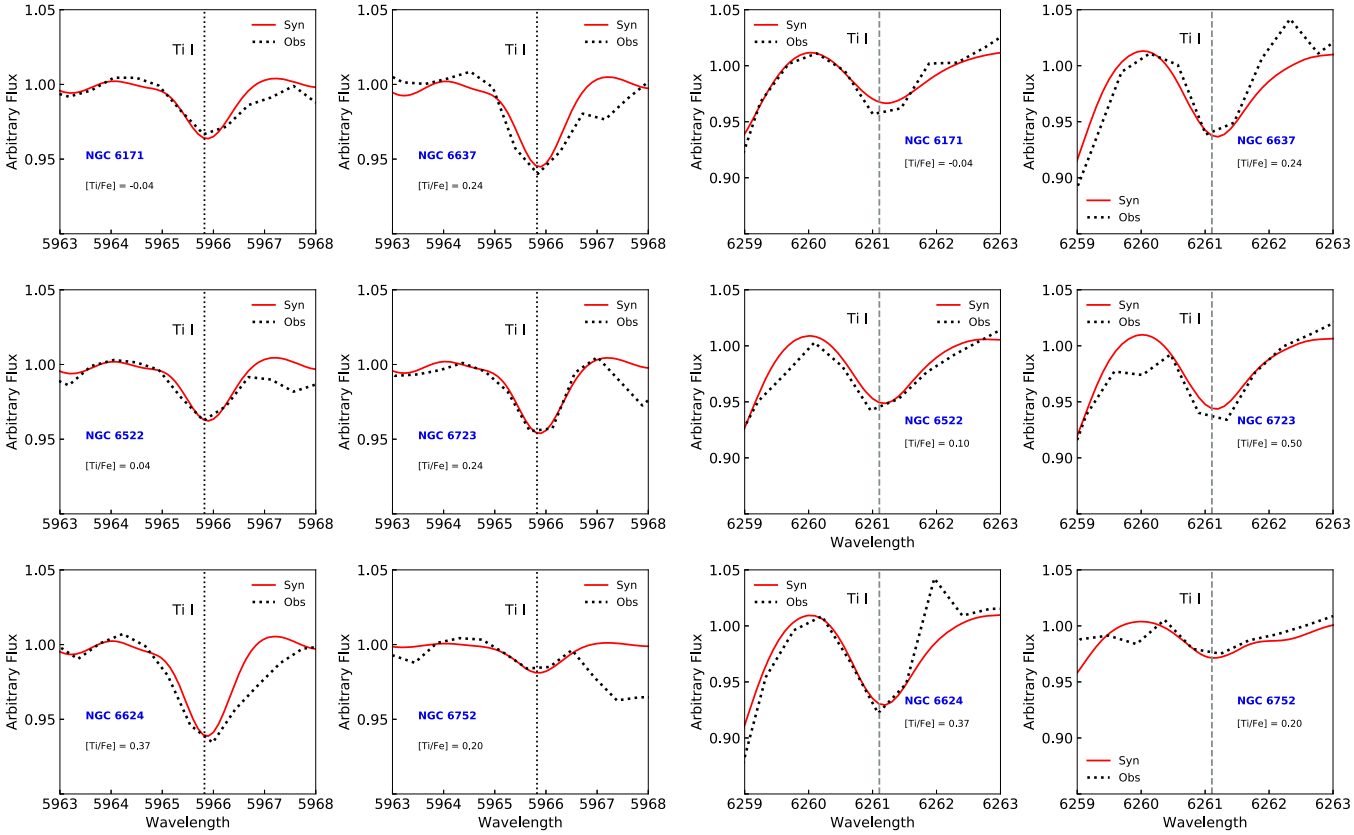

Figure 7. Fitting of synthetic to observed spectra for different regions with Ti I lines.

models (Gustafsson et al. 2008) applied to the Sun (Kurúcz 2005)[6] and Arcturus (Hinkle et al. 2000). We adopted the stellar parameters $T_{\rm eff}$, $\log g$, metallicity ([Fe/H]), and microturbulent velocity ($v_{\rm t}$) of 5770 K, 4.44, 0.0, and 1.0 km s^{-1} for the Sun, and 4275 K, 1.55, −0.54, 1.65 km s^{-1} for Arcturus, from Meléndez et al. (2003). We adopted abundances of A(Fe) = 7.50 for the Sun, and [Mg/Fe] = +0.15 and [Ca/Fe] = +0.10 for Arcturus. Note that the damping constant through the interaction constant C_6 that fit the wings of strong lines, depends on the atmospheric model grid adopted, as pointed out in Barbuy et al. (2003, their Figure 1).

Another comment regarding strong lines is that LTE calculations do not reproduce the bottom of these lines, given that they form in NLTE, and besides their formation takes place in chromospheric layers, that are not included in the usual model atmospheres.

For the Mg I triplet lines at 5167.3, 5172.68, and 5183.60 Å and CaT at 8498.023, 8542.091, and 8662.141 Å, we used the atomic constants listed in Table 4. This resulted in very good fits shown in Figures 10 and 11.

4.3. Literature Abundances

The resulting abundances derived in the above subsections are then compared with other methods of abundance derivation from integrated light reported in the literature. The element abundances derived from different methods and sources are compiled in Table 2. The method employed is identified as high-resolution spectroscopy (HRS), CMD, compilation (comp.), and from integrated spectra: equivalent widths (ISEW), full spectrum fitting (ISFF), or finally the fit of individual lines (ISfit), the latter being our adopted method.

Below we briefly describe methods employed in the literature for derivation of abundances applied to the six sample GCs. The following references and comments given here are by no means exhaustive, since there is more extensive literature addressing the clusters.

Usher et al. (2019) derived Ca abundances from EW measurements following prescriptions given in Usher et al. (2012), similarly to other studies in the literature such as Vásquez et al. (2018) applied to individual stars, or Foster et al. (2010) applied to integrated light. Usher et al. (2019) derive Ca abundances for all sample clusters in the present work and their values are given in Table 2.

Colucci et al. (2017), following earlier work by Sakari et al. (2013), measured EWs of individual lines of Mg, Ca, Ti, Cr, Ba, and Eu, from the same WAGGS spectra used here, and they report the corresponding element abundances. They also use spectrum synthesis to fit iron peak and heavy element lines that require inclusion of HFS. The cluster NGC 6752 is a common factor in Colucci et al. (2017) and the present work, noting that in most cases Colucci et al. chose different lines relative to our Table 3. In Table 5, we compare the abundances for the lines in common between Colucci et al. and the present work, for NGC 6752.

Larsen et al. (2017) obtained high-resolution integrated spectra ($R \sim 40{,}000$) of seven clusters, including NGC 6752, in common with the present work. Their method of full

[6] kurucz.harvard.edu/Sun.html

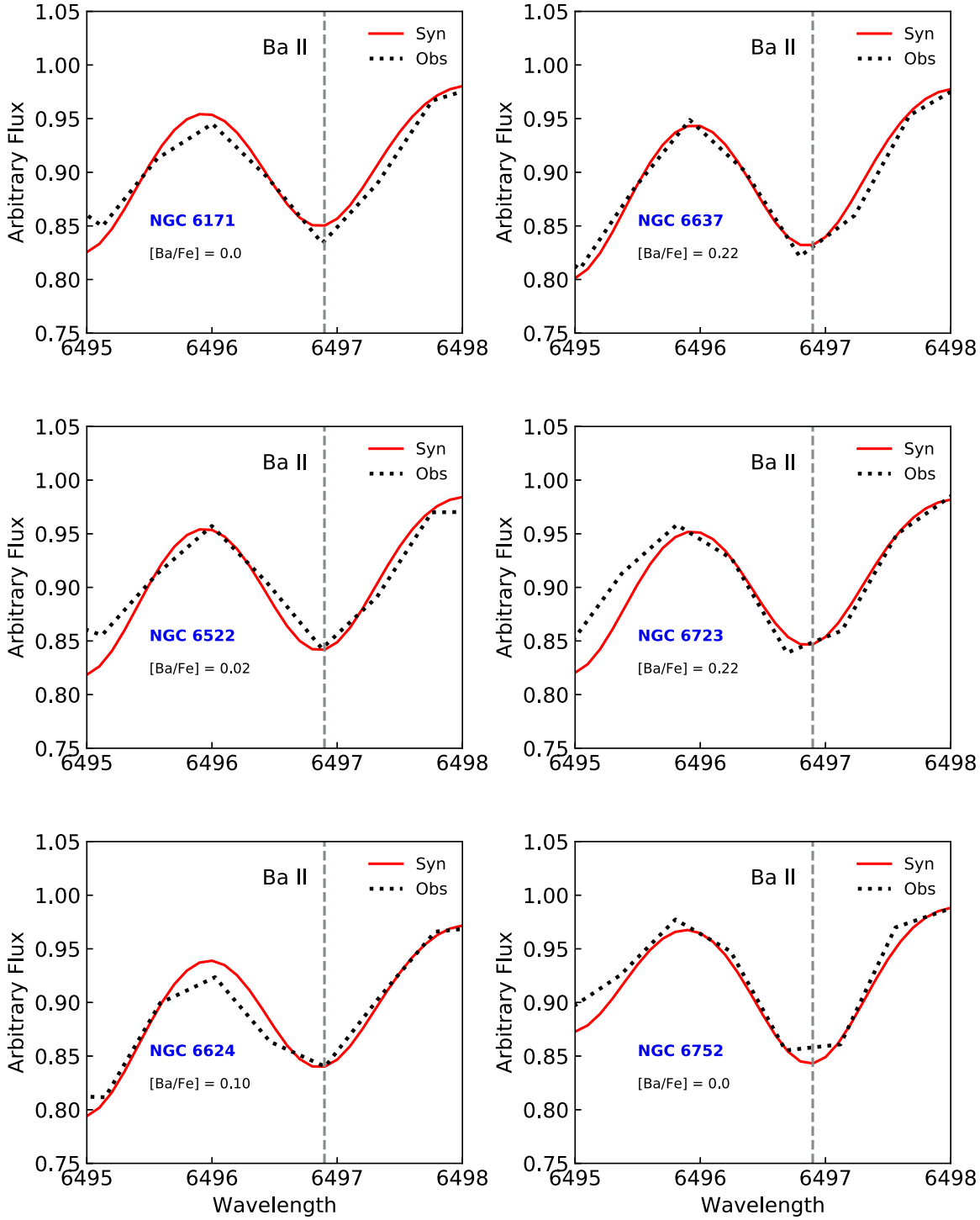

Figure 8. Observed and synthetic spectra in the region of the line 6496 Å Ba II.

spectrum synthesis, as well as the use of the Dartmouth isochrones is similar to that of the present work. They apply overall fitting to all the spectrum, finding the best abundances to fit it all, therefore in this respect, it is different from the present work where we have chosen the most reliable lines to be fitted.

Conroy et al. (2018) present a full spectrum fitting method to derive abundances from integrated spectra. They use Dartmouth isochrones and MILES empirical spectra (Sánchez-Blázquez et al. 2006), complemented by a library of spectra in the near-infrared. An important addition is the calculation of synthetic spectra with variable abundances, in order to adapt the observed spectra to response functions due to variable abundances. From fitting spectra by Schiavon et al. (2005), they derive abundances of Mg, Si, Ca, and Ti for 41 GCs, including our six sample clusters.

Table 6 reports the final mean abundance values obtained in the present work. In Figure 12 these results are compared with those from the literature listed in Table 2, for the elements Mg, Al, Si, Ca, and Ti. We do not include Na, for the reasons

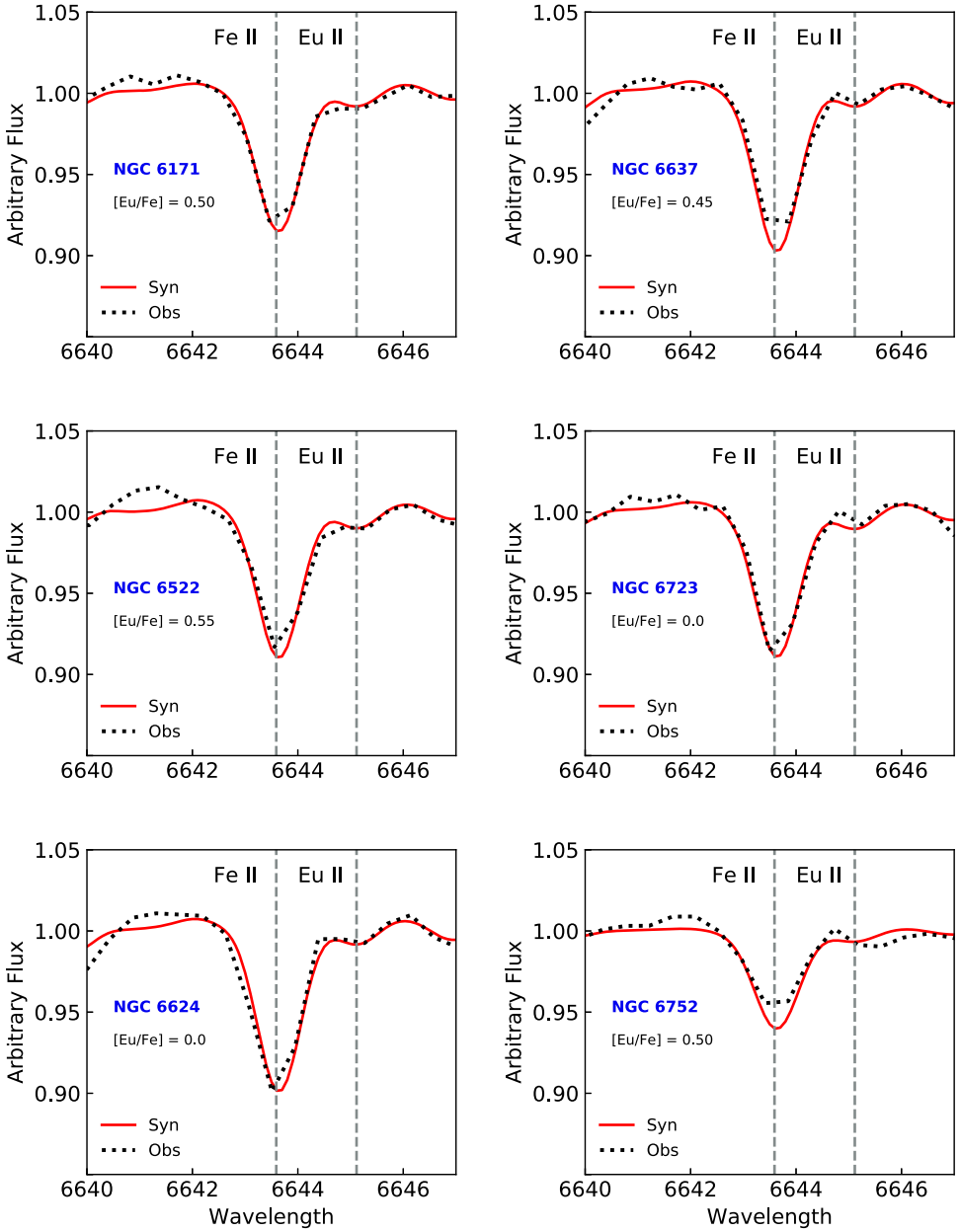

Figure 9. The 6645 Å Eu II line in the synthetic and observed spectra for each globular cluster of our sample.

explained in Section 5 (i.e., the difficulty in deriving reliable Na abundances from the lines available), or Ba and Eu because there are very few literature abundances for these elements for the sample clusters. Figure 12 shows that there is good agreement between the present results and other abundance derivations from integrated spectra—star symbols (ours) compared with squares (others). A spread of abundances is seen among different high-resolution spectroscopic analyses: for NGC 6522, the present results are in good agreement with our previous high-resolution spectroscopic analysis (Barbuy et al. 2014), and there are differences with respect to Ness et al. (2014). For NGC 6752, the high-resolution spectroscopic analysis by Carretta et al. (2012) gives abundances for its three stellar populations and a mean value is plotted in the figure. S. O. Souza et al. (2019, in preparation) found fractions of 25%, 43%, and 32% for 1G, 2G, and 3G, very similar to the proportions of 25%, 40%, and 30% obtained by Milone et al. (2013), and also adopted by Tenorio-Tagle et al. (2019), therefore a mean of abundances from the three stellar populations appears suitable. Aluminum has a high abundance, given their high abundance values for 2G and 3G stars, that we do not confirm from the integrated spectra.

In conclusion, the derivation of abundances line-by-line from integrated spectra, for a few suitable lines, does give results compatible with high-resolution spectroscopic analyses, and with other integrated spectra analyses.

5. Effects of Multiple Stellar Populations

The identification of multiple stellar populations in GCs has been recently definitively demonstrated by the so-called chromosome map method, with UV photometric data provided in Piotto et al. (2015), and explained in detail in Milone et al. (2017). For many of the present clusters, the identification of percentages of first and second stellar populations are available

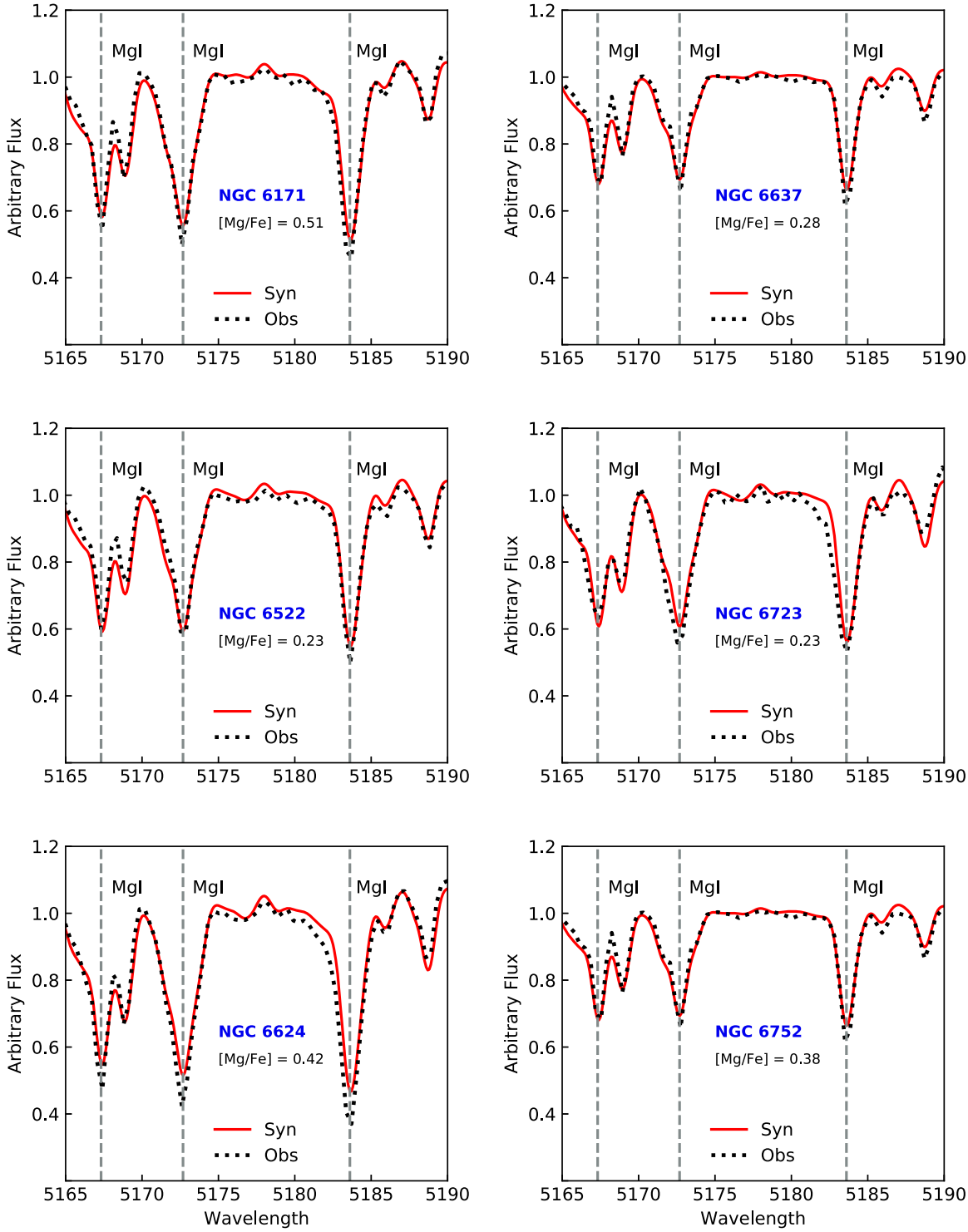

Figure 10. The Mg I triplet lines at 5167.3, 5172.68, and 5183.60 Å for the sample clusters.

in Milone et al. (2017). The reason for the chromosome map to be feasible is due to the variations in the abundances of C, N, and O, as clearly illustrated in Figure 1 by Piotto et al. (2015).

The presence of multiple stellar populations together with variations in abundances of C, N, O, Na, Al, and Mg was identified and described in Carretta et al. (2009), Gratton et al. (2012), Renzini et al. (2015), and Bastian & Lardo (2018), among others. Anticorrelations Na–O and Mg–Al are observed, where in particular the Na–O behavior has been extensively documented (Carretta 2019; Carretta et al. 2009). Note that for C, N, and O, other effects such as stellar evolution along the RGB also affect their abundances.

Na overabundances—The main effect in abundances of second generation stars is the Na–O anticorrelation as shown in Carretta et al. (2009) and Carretta (2019) for a sample of GCs. In second generation stars, Na is enhanced by amounts between 0.2 and 0.7

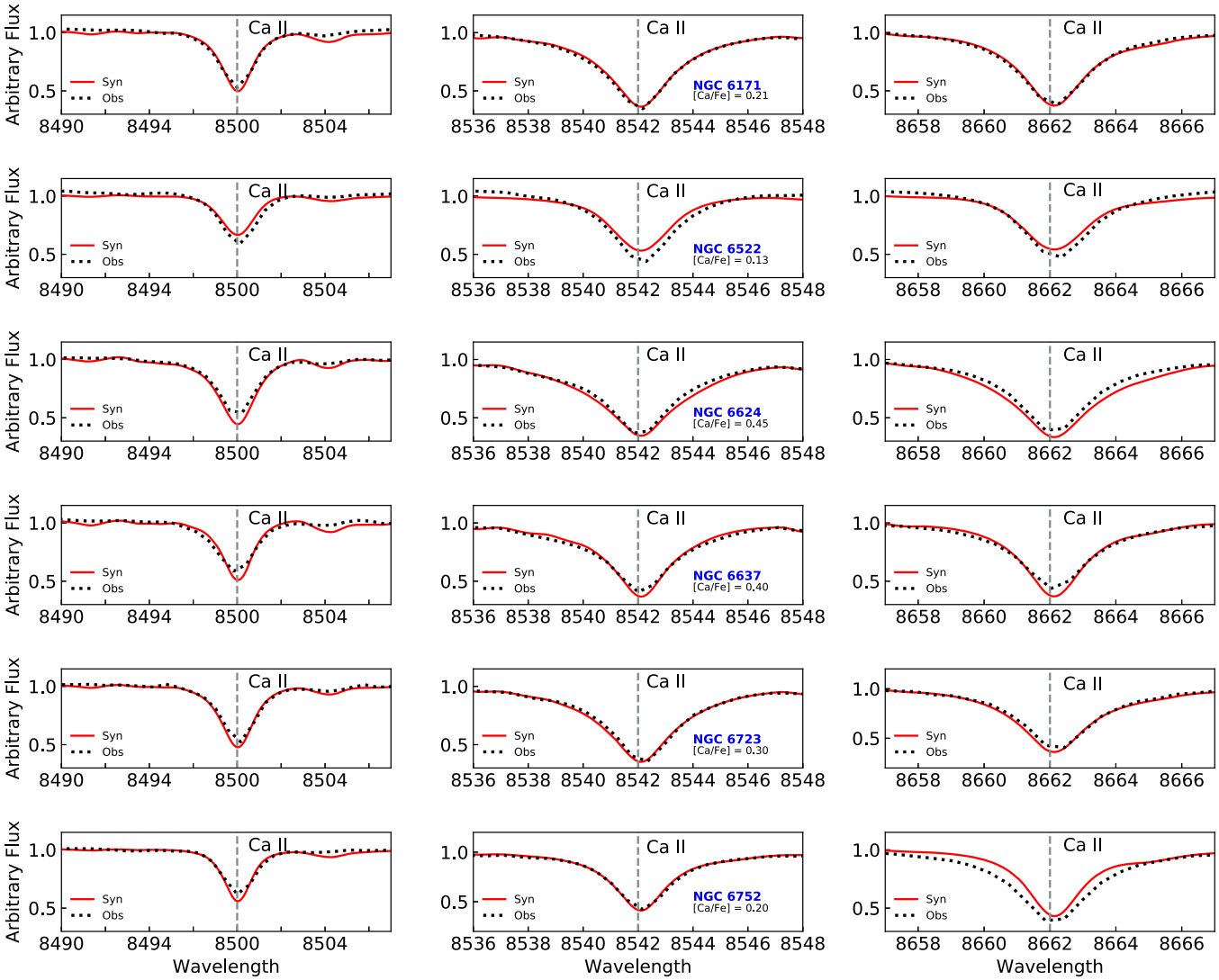

Figure 11. Ca II triplet lines for the sample clusters.

(Campbell et al. 2013), whereas oxygen is depleted. The proportions of first generation stars relative to total $N_1/N_{\rm total}$ were measured by Milone et al. (2017), and confirmed in R. A. P. Oliveira et al. (2019, in preparation), in a first approximation, as given in Table 1. If only bonafide members of first and second generations are taken into account, the proportions can change in some cases (R. A. P. Oliveira et al. 2019, in preparation). For the case of NGC 6522, according to Kerber et al. (2018), 84% of the stellar population belongs to a second generation, therefore its first generation fraction should be around $N_1/N_{\rm total} = 0.160$. In most cases, the second generation is dominant, and this should be seen in the integrated spectra.

Figure 13 shows the fit of three doublets of Na I, assuming a mean [Na/Fe] = 0.0 and +0.35, for lines in NGC 6723. These values are chosen from Table 2 where the highest mean values of [Na/Fe] = 0.35 are given for some of the sample clusters. The graph for NGC 6723, exemplifies the difficulty in establishing which is the mean Na abundance. The line Na I 5682.63 Å is inconclusive, line 8194.79 Å indicates [Na/Fe] = 0.0, whereas 5688.20, 6154.23, and 6160.75 Å indicate that [Na/Fe] = +0.35, and 8183.26 Å is in between. In Table 7 we report the indication of mean Na abundance from this set of lines for the sample clusters. The conclusion is that the present data do not allow us to draw firm evidence of second generation stars signatures, and that higher S/N and higher resolution data would probably allow such a procedure.

Other elements that could be indicators of multiple stellar populations, Mg and Al, are normally enhanced as found in bulge stars (McWilliam 2016; Barbuy et al. 2018a). It would be possible to infer multiple stellar population evidence for a cluster or galaxy if Na is very high and/or Mg is very low.

IMF and enhancements of Na and TiO features—Note that Na enhancements are also used to derive evidence on bottom-heavy IMFs (Conroy & van Dokkum 2012). As concerns Na, given that in our Galactic bulge there is no evidence of IMF variations (Wegg et al. 2017; Barbuy et al. 2018a), we assume standard IMF throughout this paper. We believe that Na lines are probably not suited for IMF deduction, given the effects not only of multiple stellar populations discussed in the previous subsection, but also because Na can be enhanced in the central parts of galaxies, as it apparently is in our Galactic bulge (Lecureur et al. 2007; Barbuy et al. 2018a).

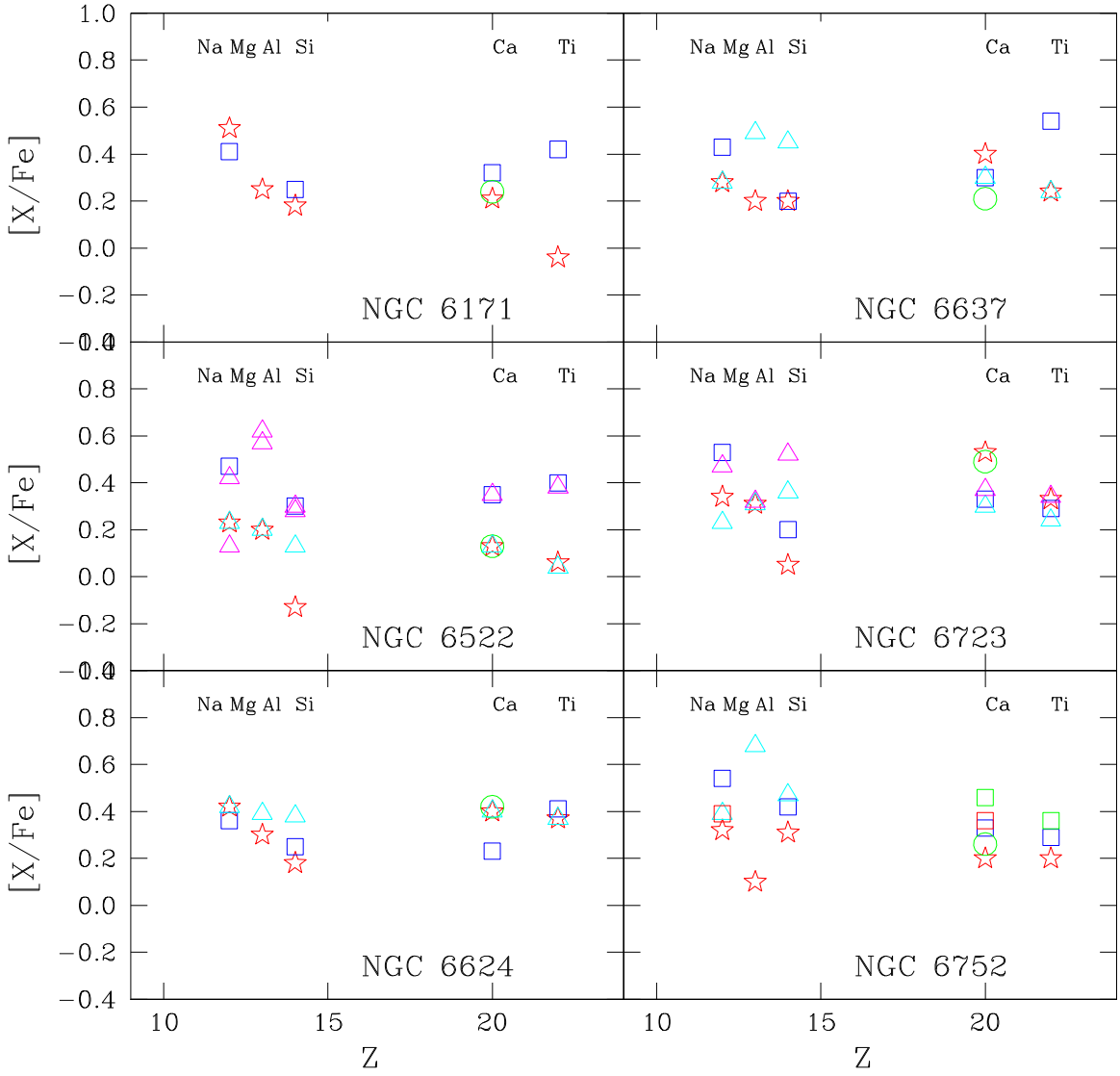

Figure 12. [X/Fe] vs. element number *Z*. Symbols given in all panels: present results: red open stars; Conroy et al. (2018): blue open squares; Usher et al. (2019): green open circles. Other symbols: cyan open triangles: Barbuy et al. (2014), Valenti et al. (2011), Lee (2007), Rojas-Arriagada et al. (2016), and Carretta et al. (2012); magenta open triangles: Ness et al. (2014) and Crestani et al. (2019); green open squares: Colucci et al. (2017); red open squares: Larsen et al. (2017).

Table 5
Comparison of Abundances Line-by-line with Colucci et al. (2017) for NGC 6752, Assuming Their [Fe/H] = −1.58

Species	λ (Å)	A (X)$_{\odot\text{Colucci}}$	A (X)$_{\text{Colucci}}$	[X/Fe]$_{\text{Colucci}}$	[X/Fe]$_{\text{thiswork}}$
Na I	5682.633	6.44	4.95	+0.09	+0.00
Na I	5688.200	6.34	4.75	−0.01	+0.35
Mg I	5528.405	7.52	6.05	+0.11	+0.38
Mg I	5711.088	7.58	5.95	−0.05	+0.25
Si I	7405.79	7.56	6.56	+0.58	+0.47
Si I	7415.96	7.63	6.46	+0.41	+0.47
Si I	7423.51	7.60	6.26	+0.24	+0.00
Ca I	6162.167	6.40	5.06	+0.24	+0.20
Ca I	6166.440	6.36	5.16	+0.38	+0.20
Ca I	6439.080	6.02	4.96	+0.52	+0.20
Ti I	5866.449	5.04	4.00	+0.54	+0.20
Ba II	6496.90	2.18	0.73	+0.13	0.00

Studies on IMF variations are deduced, besides studies using Na lines, also from TiO and Wing-Ford FeH bands (La Barbera et al. 2016). The FeH bands are located around 1 μm (Schiavon et al. 1997), therefore out of the range of the present data. TiO bands can be investigated with the present method. We tried to compute TiO bands at 7000–7500 Å, as

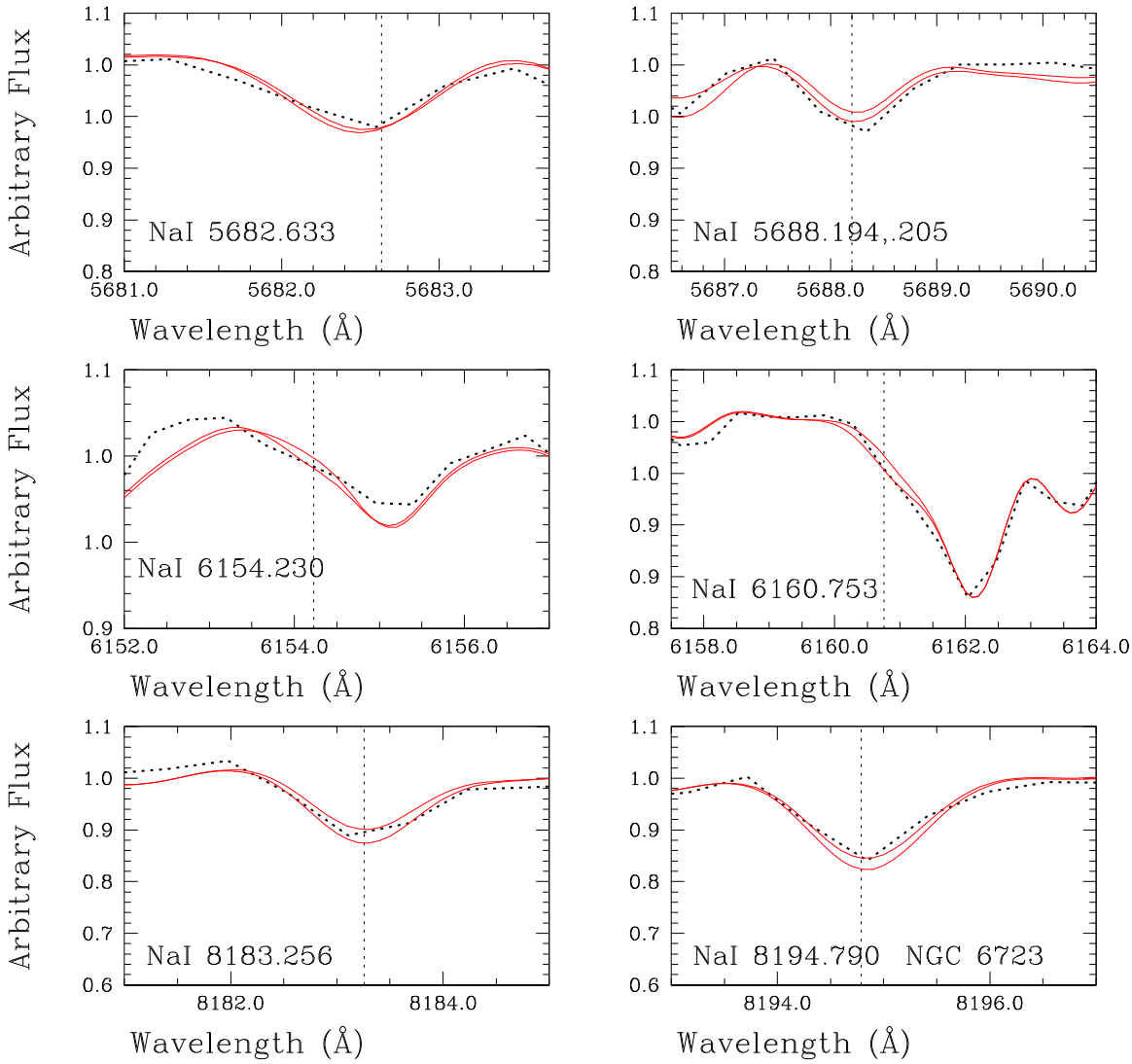

Figure 13. The observed and synthetic spectra for NGC 6723 of Na I lines: (a) 5682 Å and 5688 Å; (b) 6154 and 6160 Å; and (c) 8183 and 8194 Å, computed with [Na/Fe] = 0.0 and 0.35.

Table 6
Adopted Metallicities and Resulting Mean Abundances for the Elements: Mg, Al, Si, Ca, Ti, Ba, and Eu. Na is given in Table 7

Cluster	[Fe/H]	[Mg/Fe]	[Al/Fe]	[Si/Fe]	[Ca/Fe]	[Ti/Fe]	[Ba/Fe]	[Eu/Fe]
6171	−1.02	0.51	0.25	0.18	0.21	−0.04	0.00	0.50
6522	−0.95	0.23	0.20	−013	0.13	0.06	0.02	0.55
6624	−0.69	0.42	0.30	0.18	0.40	0.37	0.10	0.00
6637	−0.77	0.28	0.20	0.20	0.40	0.24	0.22	0.45
6723	−0.98	0.34	0.31	0.05	0.53	0.33	0.22	0.00
6752	−1.53	0.32	0.10	0.31	0.20	0.20	0.00	0.50

previously exemplified in Milone et al. (1995), applied to the most metal-rich cluster in our sample, NGC 6624. However, at this metallicity the bands are not strong enough to be inspected.

Helium abundances—We have adopted isochrones with primordial helium abundances, that in the DSED isochrones correspond to $Y = 0.247$. Despite detection of a small helium enchancement in second generation stars for these clusters by Lagioia et al. (2018) and Milone et al. (2018, 2019), the effects on the CMDs, for our purposes, are negligible. The He enhancement in 2G stars of the sample clusters, from Milone et al. (2019), are reported in Table 1. The enhancements are small, therefore the isochrones for 2G, if He enhancement was to be taken into account, would be very close to the 1G enhancement. Essentially, if enhanced He is assumed, there is a small decrease in age. S. O. Souza et al. (2019, in preparation) have studied the three stellar populations in NGC 6752,

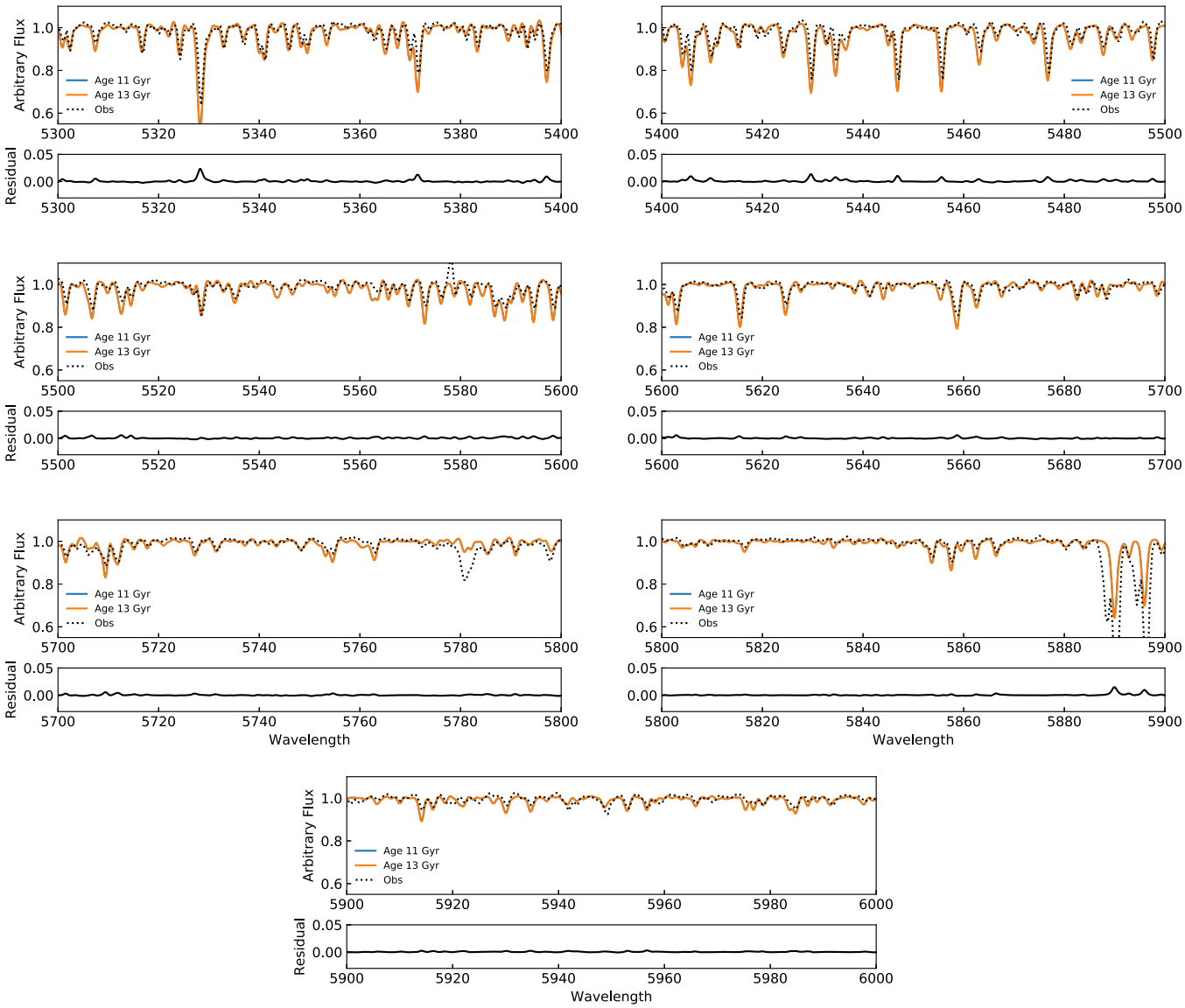

Figure 14. NGC 6522: Synthetic spectra for ages of 11 and 13 Gyr in the region $\lambda\lambda$ 5300–6000 Å, and respective residuals in the lower panels.

Table 7
Na Abundance from the Main Na I Lines in the Integrated Spectra

Cluster	5682.63 Å	5688.20 Å	6154.23 Å	6160.75 Å	8183.25 Å	8194.79 Å
NGC 6171	0.00	0.35	0.35	0.00	0.35	0.20
NGC 6522	0.00	0.35	0.20	0.00	0.20	0.20
NGC 6624	0.20	0.35	0.35	0.35	0.00	0.20
NGC 6637	0.00	0.35	0.35	0.00	0.00	0.00
NGC 6723	⋯	0.35	0.35	0.35	0.20	0.00
NGC 6752	0.00	0.35	⋯	0.35	0.20	0.35

assuming $Y = 0.247$, 0.257, and 0.288, established by Milone et al. (2019), and found ages of 13.4, 13.2, and 13.0 Gyr for 1G, 2G, and 3G, respectively.

Therefore, the effects of helium enhancements can be treated in terms of younger ages, as described in the next section.

Effects of age—It is well-known that the effect of age in a CMD is the magnitude of the turn-off point, which is brighter for younger ages. In the integrated spectra there is little change in the lines, given that the RGB stars dominate the flux. This is shown in Figure 14, with the comparison of spectra between 11 and 13 Gyr for NGC 6522, together with the residuals.

6. Conclusions

We have built the code SynSSP that combines isochrones for a given age, metallicity, helium abundance, and [α/Fe], to calculations of a series of synthetic spectra. We are able to

reproduce the integrated spectra of very old GCs in the metallicity range $-1.6 < [Fe/H] < -0.7$.

The main aim of this work is to be able to reproduce the integrated spectra of well-known GCs, in order to be able to use this method of building integrated spectra for the analysis of extragalactic GCs, such as those developed by Sakari et al. (2014).

From the present analysis, we can conclude:

1. It is possible to reproduce prominent lines of Na, Mg, Al, Si, Ca, Ti, Ba, and Eu, to derive their abundances from the integrated spectra, which are in good agreement with previous results in the literature. This opens the possibility to apply this method to distant star clusters in other galaxies.
2. With the abundances of the most important elements being derived, it is expected that the residual difference between observed and synthetic integrated spectra will be reduced.
3. The effect of age is small among old star clusters. For younger star clusters, they would be distinguishable due to their bluer colors, and by the presence of other sets of lines.
4. The effect of helium enhancement in second (and subsequent) stellar generations is a somewhat younger age, therefore this effect can be neglected.

Finally, a further objective of this work for the future is to use a combination of integrated spectra of SSPs, well-tested with our method, in the building of spectra of galaxies.

T.C.M. acknowledges the post-doctoral FAPESP fellowship No. 2018/03480-7. M.T. thanks the support of CNPq, process number 307675/2018-1. B.B. acknowledges FAPESP project 2014/18100-4 and partial financial support from CAPES Financial project 001 and CNPq. S.R. acknowledge financial support from FAPESP, process number 2015/50374-0 and partial financial support from CAPES Financial project 001 and CNPq.

Appendix
Synthetic Spectra—NGC 6522

The full spectral synthesis performed for NGC 6522 in the spectral range of 4500 to 9000 Å (red lines) are compared to the observed from the WAGGS catalog (Figures 15–19; Usher et al. 2017).

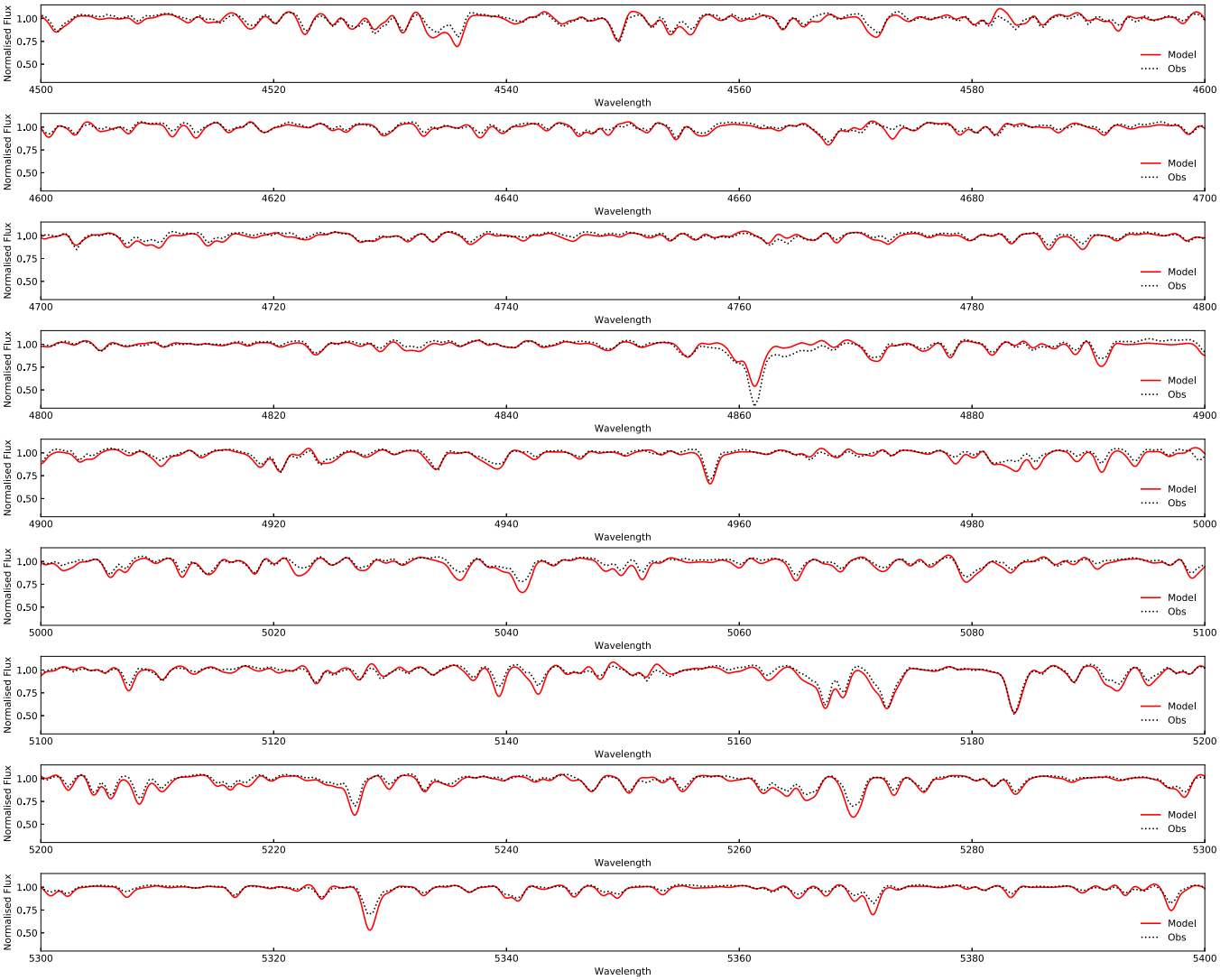

Figure 15. Observed and synthetic spectra for the cluster NGC 6522 in the range 4500–5400 Å. Main absorption lines are highlighted.

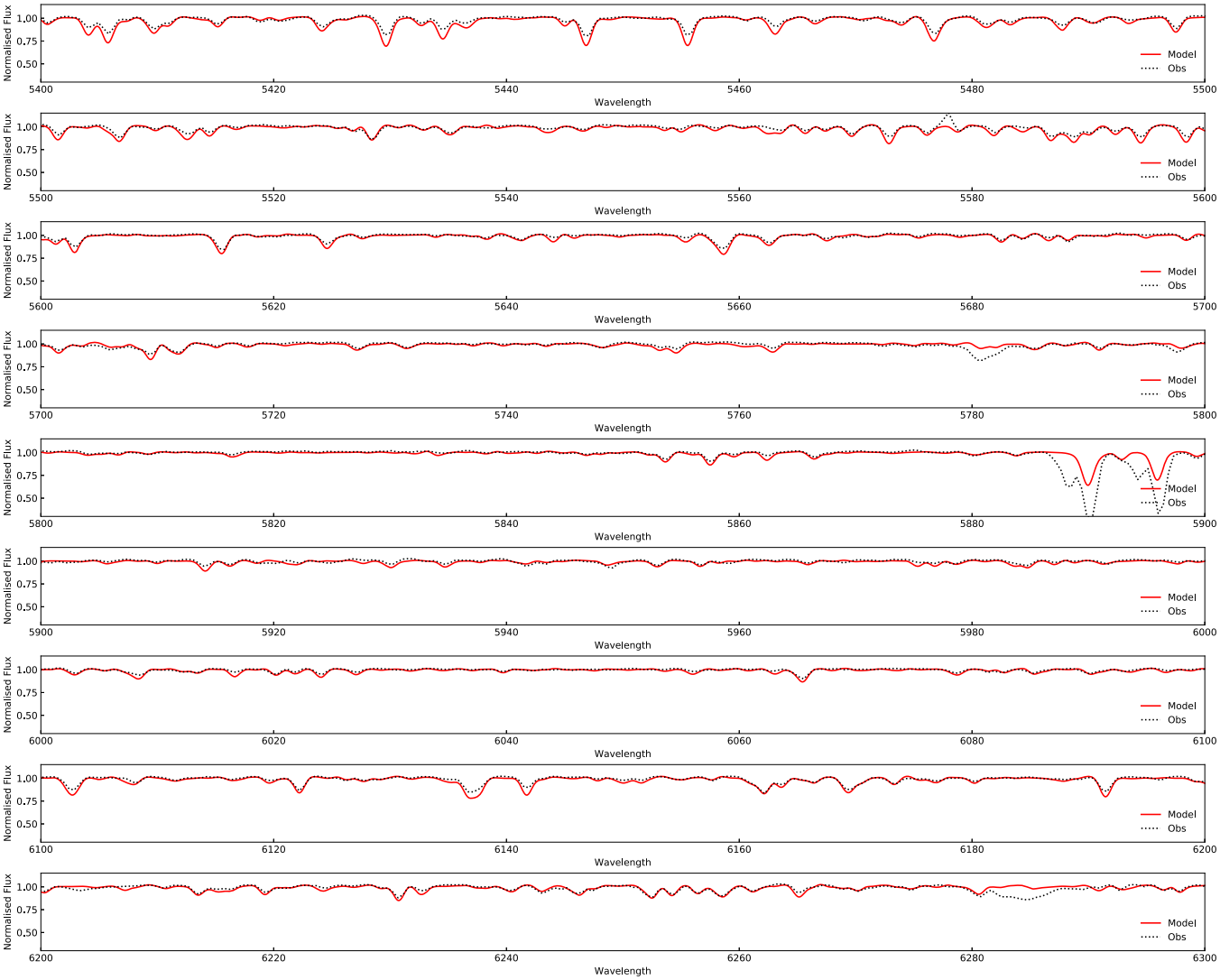

Figure 16. Continuation of Figure 15 for spectra in the range 5400–6300 Å. The gray areas represent the region of the telluric line.

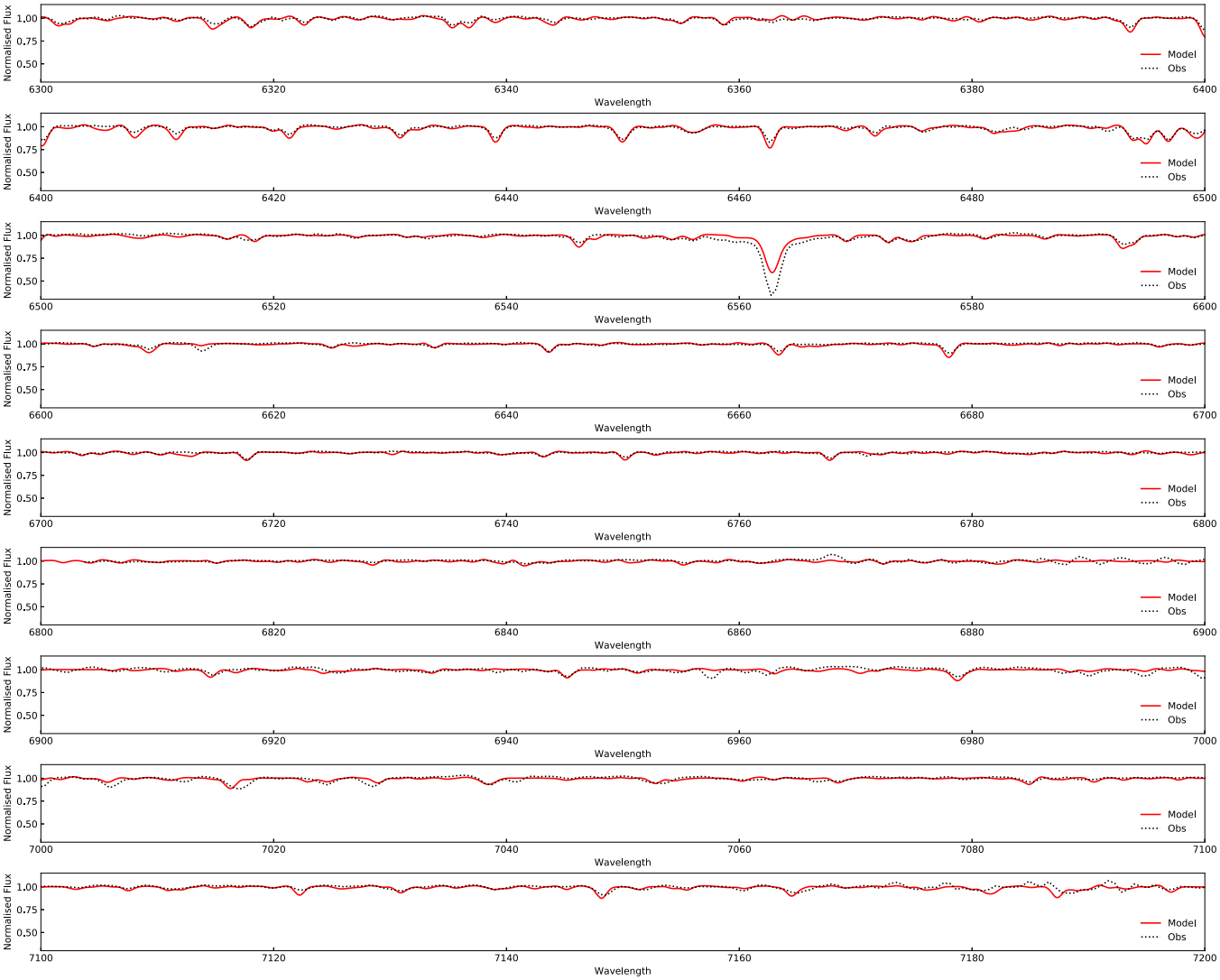

Figure 17. Same as Figure 16 for the wavelength range 6300–7200 Å.

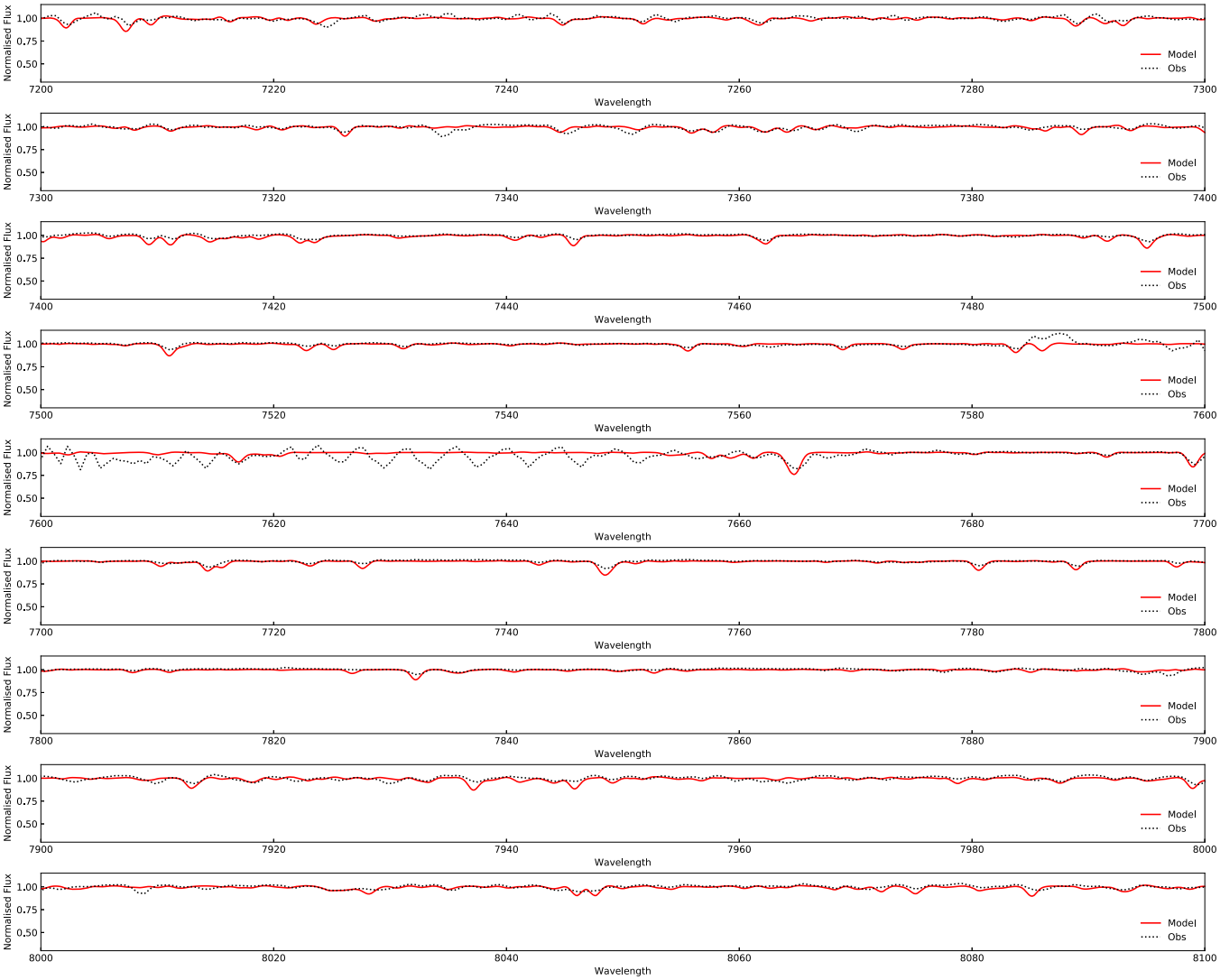

Figure 18. Same as Figure 17 for the wavelength range 7200–8100 Å.

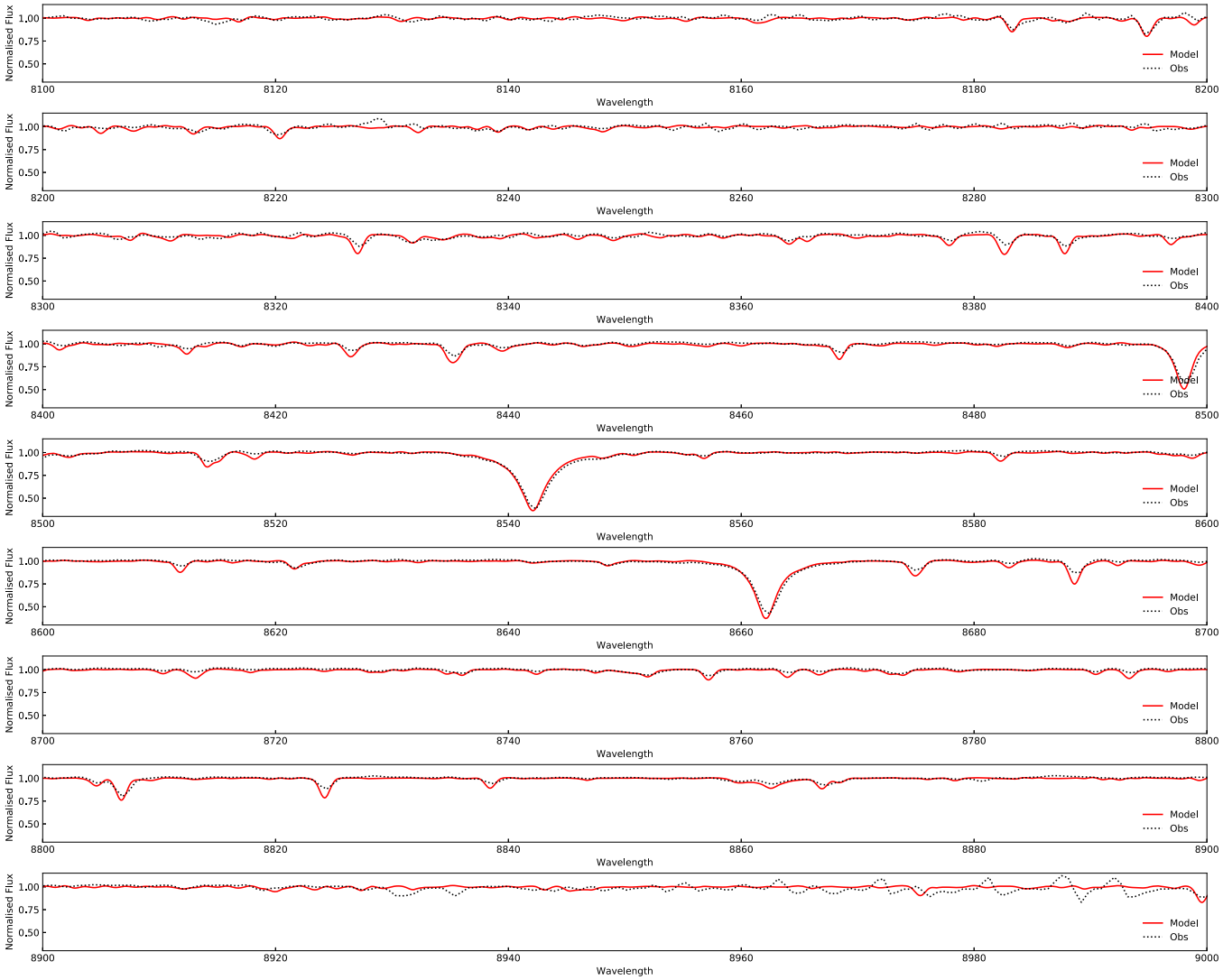

Figure 19. Synthetic and observed spectra for NGC 6522 in the wavelength range 8100–9000 Å.

ORCID iDs

T. C. Moura https://orcid.org/0000-0003-1548-7221
M. Trevisan https://orcid.org/0000-0001-7309-8609
B. Barbuy https://orcid.org/0000-0001-9264-4417
S. Rossi https://orcid.org/0000-0001-7479-5756

References

Barbuy, B. 1982, PhD thesis, Université de Paris VII
Barbuy, B., Chiappini, C., Cantelli, E., et al. 2014, A&A, 570, A76
Barbuy, B., Chiappini, C., & Gerhard, O. 2018a, ARA&A, 56, 223
Barbuy, B., Perrin, M.-N., Katz, D., et al. 2003, A&A, 404, 661
Barbuy, B., Trevisan, J., & de Almeida, A. 2018b, PASA, 35, 46
Bastian, N., & Lardo, C. 2018, ARA&A, 56, 83
Bica, E., & Alloin, D. 1986, A&A, 162, 21
Bica, E., Ortolani, S., & Barbuy, B. 2016, PASA, 33, 28
Campbell, S. W., D'Orazi, V., Yong, D., et al. 2013, Natur, 498, 198
Carretta, E. 2019, A&A, 624, A24
Carretta, E., Bragaglia, A., Gratton, R. G., Lucatello, S., & D'Orazi, V. 2012, ApJL, 750, L14
Carretta, E., Bragaglia, A., Gratton, R. G., et al. 2009, A&A, 505, 117
Cayrel, R., Perrin, M.-N., Barbuy, B., & Buser, R. 1991, A&A, 247, 108
Chmielewski, Y. 2000, A&A, 353, 666
Coelho, P., Barbuy, B., Meléndez, J., Schiavon, R. P., & Castilho, B. V. 2005, A&A, 443, 735
Colucci, J. E., Bernstein, R. A., & McWilliam, A. 2017, ApJ, 834, 105
Conroy, C., & van Dokkum, P. G. 2012, ApJ, 760, 71
Conroy, C., Villaume, A., van Dokkum, P. G., & Lind, K. 2018, ApJ, 854, 139
Crestani, J., Alves-Brito, A., Bono, G., Puls, A. A., & Alonso-Garcia, J. 2019, MNRAS, 487, 5463
Dias, B., Barbuy, B., Saviane, I., et al. 2015, A&A, 573, A13
Dias, B., Barbuy, B., Saviane, I., et al. 2016, A&A, 590, A9
Dotter, A., Chaboyer, B., Jevremović, D., et al. 2008, ApJS, 178, 89
Fernández-Trincado, J. G., Zamora, O., Souto, D., et al. 2019, A&A, 627, 178
Foster, C., Forbes, D. A., Proctor, R. N., et al. 2010, ApJ, 139, 1566
Gratton, R. G., Carretta, E., & Bragaglia, A. 2012, A&ARv, 20, 50
Gratton, R. G., Lucatello, S., Sollima, A., et al. 2015, A&A, 573, A92
Gray, D. F. 2005, The Observation and Analysis of Stellar Photospheres (Cambridge: Cambridge Univ. Press)
Gustafsson, B., Edvardsson, B., Eriksson, K., et al. 2008, A&A, 486, 951
Harris, W. E. 1996, AJ, 112, 1487
Hinkle, K., Wallace, L., Valenti, J., & Harmer, D. 2000, Visible and Near Infrared Atlas of the Arcturus Spectrum 3727–9300 A (San Francisco, CA: ASP)
Kerber, L., Nardiello, D., Ortolani, S., et al. 2018, ApJ, 853, 15
Kroupa, P. 2001, MNRAS, 322, 231
Kurúcz, R. L. 2005, MSAIS, 8, 189
La Barbera, F., Ferreras, I., Vazdekis, A., et al. 2013, MNRAS, 433, 3017
La Barbera, F., Vazdekis, A., Ferreras, I., et al. 2016, MNRAS, 457, 1468
Lagioia, E. P., Milone, A. P., Marino, A. F., et al. 2018, MNRAS, 475, 4088
Larsen, S. S., Brodie, J. P., & Strader, J. 2017, A&A, 601, A96
Lecureur, A., Hill, V., Zoccali, M., et al. 2007, A&A, 465, 799

Lee, J.-W. 2007, RMxAC, 28, 120
Martins, L. P., Lima-Dias, C., Coelho, P. R. T., & Laganá, T. 2019, MNRAS, 484, 2388
McWilliam, A. 2016, PASA, 33, 40
Meléndez, J., Barbuy, B., Bica, E., et al. 2003, A&A, 411, 417
Milone, A., Barbuy, B., & Bica, E. 1995, A&AS, 113, 547
Milone, A. P., Marino, A. F., Bedin, L. R., et al. 2019, MNRAS, 484, 4046
Milone, A. P., Marino, A. F., Piotto, G., et al. 2013, ApJ, 767, 120
Milone, A. P., Marino, A. F., Renzini, A., et al. 2018, MNRAS, 481, 5098
Milone, A. P., Piotto, G., Renzini, A., et al. 2017, MNRAS, 464, 3636
Ness, M., Asplund, M., & Casey, A. R. 2014, MNRAS, 445, 2994
Pehlivan Rhodin, A., Hartman, H., Nilsson, H., & Jönsson, P. 2017, A&A, 598, A102
Piotto, G., Milone, A. P., Bedin, L. R., et al. 2015, AJ, 149, 91
Pritzl, B. J., Venn, K., & Irwin, M. 2005, AJ, 130, 2140
Renzini, A., D'Antona, F., Cassisi, S., et al. 2015, MNRAS, 454, 4197
Roediger, J. C., Courteau, S., Graves, G., & Schiavon, R. P. 2014, ApJS, 210, 10
Rojas-Arriagada, A., Zoccali, M., Vásquez, S., et al. 2016, A&A, 587, A95
Ryabchikova, T., Piskunov, N., Kurucz, R. L., et al. 2015, PhyS, 90, 054005
Sakari, C. M., Shetrone, M., Venn, K., McWilliam, A., & Dotter, A. 2013, MNRAS, 434, 358
Sakari, C. M., Venn, K., Shetrone, M., Dotter, A., & Mackey, D. 2014, MNRAS, 443, 2285
Salpeter, E. E. 1955, ApJ, 121, 161
Sánchez-Blázquez, P., Peletier, R. F., Jiménez-Vicente, J., et al. 2006, MNRAS, 371, 703
Saviane, I., Da Costa, G. S., Held, E. V., et al. 2012, A&A, 540, A27
Schiavon, R. P., Barbuy, B., & Singh, P. D. 1997, ApJ, 484, 499
Schiavon, R. P., Rose, J. A., Courteau, S., & MacArthur, L. 2005, ApJS, 160, 163
Smith, G., & Drake, J. J. 1988, MNRAS, 231, 115
Tenorio-Tagle, G., Silich, S., Palouš, J., Muñoz-Tuñón, C., & Wünsch, R. 2019, ApJ, 879, 58
Trager, S. C., Worthey, G., Faber, S. M., Burstein, D., & González, J. J. 1998, ApJS, 116, 1
Usher, C., Beckwith, T., Bellstedt, S., et al. 2019, MNRAS, 482, 1275
Usher, C., Forbes, D. A., Brodie, J., et al. 2012, MNRAS, 426, 1475
Usher, C., Pastorello, N., Bellstedt, S., et al. 2017, MNRAS, 468, 3828
Valenti, E., Origlia, L., & Rich, R. M. 2011, MNRAS, 414, 2690
VandenBerg, D. A., Brogaard, K., Leaman, R., & Casagrande, L. 2013, ApJ, 775, 134
Vásquez, S., Saviane, I., Held, E. V., et al. 2018, A&A, 619, A13
Wegg, C., Gerhard, O., & Portail, M. 2017, ApJL, 843, L5